Eur. Phys. J. A (2016) **52**: 7
DOI 10.1140/epja/i2016-16007-4

THE EUROPEAN PHYSICAL JOURNAL A

Regular Article – Experimental Physics

High-precision measurement of the associated strangeness production in proton-proton interactions

The COSY-TOF Collaboration

S. Jowzaee[1,7], E. Borodina[1], H. Clement[4,6], E. Doroshkevich[5,6,a], R. Dzhygadlo[1,b], K. Ehrhardt[5,6], W. Eyrich[4], W. Gast[1], A. Gillitzer[1], D. Grzonka[1], F. Hauenstein[1,4], P. Klaja[1,4], L. Kober[4], K. Kilian[1], M. Krapp[4], M. Mertens[1,c], P. Moskal[7], J. Ritman[1,2,8], E. Roderburg[1,d], M. Röder[1,e], W. Schroeder[9], T. Sefzick[1], J. Smyrski[7], P. Wintz[1], and P. Wüstner[3]

[1] Institut für Kernphysik, Forschungszentrum Jülich, 52428 Jülich, Germany
[2] Jülich Aachen Research Allianz, Forces and Matter Experiments (JARA-FAME), Germany
[3] Zentralinstitut für Engineering, Elektronik und Analytik, 52428 Jülich, Germany
[4] Friedrich-Alexander-Universität Erlangen-Nürnberg, 91058 Erlangen, Germany
[5] Physikalisches Institut der Universität Tübingen, Auf der Morgenstelle 14, 72076 Tübingen, Germany
[6] Kepler Center for Astro and Particle Physics, University of Tübingen, Auf der Morgenstelle 14, 72076 Tübingen, Germany
[7] Institute of Physics, Jagellonian University, PL-30-348 Cracow, Poland
[8] Experimentalphysik I, Ruhr-Universität Bochum, 44780 Bochum, Germany
[9] Corporate Development, Forschungszentrum Jülich, 52428 Jülich, Germany

Received: 14 September 2015 / Revised: 25 November 2015
Published online: 15 January 2016 – © Società Italiana di Fisica / Springer-Verlag 2016
Communicated by P. Salabura

Abstract. A new high-precision measurement of the reaction pp $\rightarrow$ pK$^+\Lambda$ at a beam momentum of 2.95 GeV/c with more than 200 000 analyzed events allows a detailed analysis of differential observables and their inter-dependencies. Correlations of the angular distributions with momenta are examined. The invariant mass distributions are compared for different regions in the Dalitz plots. The cusp structure at the NΣ threshold is described with the Flatté formalism and its variation in the Dalitz plot is analyzed.

1 Introduction

The associated strangeness production of kaon and lambda is the energetic lowest possibility of creating particles with open strangeness in nucleon-nucleon collisions. This elementary reaction is of fundamental interest as it involves the dissociation of an s$\bar{\text{s}}$ quark pair into two hadrons with s = 1 and s = −1.

The creation or dissociation of the s$\bar{\text{s}}$ quark pair is described in different models by the exchange of a meson between the incoming nucleons. In most models kaon or pion exchange is assumed, but this approach can be extended to η, ρ, and ω mesons and to the strange K* mesons [1–5]. To separate the contributions of the strange and non-strange meson exchange experimentally, two possibilities are proposed: First significant differences of the analyzing power and the spin transfer coefficient for both exchanges are predicted [2]. Secondly the evidence of nucleon resonances in the lambda-kaon subsystem can only be explained by non-strange meson exchange [6].

The associated strangeness production in proton-proton collisions has been extensively studied by the DISTO Collaboration [7], the COSY-TOF Collaboration [8, 9], close to threshold by the COSY11 Collaboration [10], and at a higher beam momentum by the HADES Collaboration [11]. In spite of this large experimental data base no conclusive solution has been found on the exchange mechanism. While measurements of the spin transfer coefficient of the DISTO experiment indicate kaon exchange, COSY-TOF measurements yield a large N* contribution [8], which is a sign for dominant pion exchange.

Apart from the reaction mechanism itself, the associated strangeness production offers powerful tools to study a) the decay of N* resonances into channels with strangeness,

[a] *Present address*: Institute for Nuclear Research Moscow 117312, Russia.
[b] *Present address*: Hadron Physics I, GSI Helmholtzzentrum für Schwerionenforschung GmbH.
[c] *Present address*: Universität Duisburg-Essen 45141 Essen, Germany.
[d] e-mail: `e.roderburg@fz-juelich.de` (Corresponding author)
[e] *Present address*: Corporate Development, Forschungszentrum Jülich, 52428 Jülich, Germany.

b) the hyperon-nucleon interaction, and c) the coupled-channel effect of ($N\Lambda \leftrightarrow N\Sigma$) at the $N\Sigma$ threshold.

a) The first evidence for the creation of N* resonances in the associated strangeness production were found by comparing the Dalitz plot distributions measured with the COSY-TOF experiment [8,12] with predictions, which assume a strong impact of the resonances N(1650), N(1710), and N(1720). Further insight to the weight of these resonances and their branching ratio to the $K\Lambda$ channel can be obtained by a partial wave analysis, with precise data —including polarization observables— as input. Therefore, a combined analysis of all existing data with the Bonn-Gatchina partial wave analysis program [13] has been started [14]. First results of the partial wave analysis of HADES data are given in [15].

b) The invariant mass distributions of the associated strangeness production allows the interaction of the involved particles to be studied as a function of the relative energy in the range from zero to several hundred MeV. Especially the measurement of the nucleon-hyperon invariant mass distributions starting from zero interaction energy enables the determination of the nucleon hyperon scattering length [16,17]. The effective $p\Lambda$ scattering length has been determined from COSY-TOF data [18]. A precise knowledge of the N* resonances is needed, as they influence the $p\Lambda$ invariant mass spectrum by reflections of the $K\Lambda$ channel, thus limiting the precision of the scattering length determination.

c) The last tool provided by the associated strangeness production is to study the coupled-channel effect at the threshold of $N\Sigma$ in the nucleon-hyperon invariant mass distribution. The cusp structure at the threshold was discovered in 1961 by a bubble chamber measurement of K^- absorption in deuteron leading to $p\Lambda\pi^-$ [19]. This was confirmed by higher statistic measurements of the same reaction [20,21]. The measurements were described by different models and calculations [22–24]. As for the $pK\Lambda$ final state both thresholds of $N\Sigma$ and $K\Sigma$ have to be exceeded, the cusp effect can be observed for beam momenta above 2.7 GeV/c. First evidences for a cusp in this final state at beam momenta of 2.75 GeV/c and 2.85 GeV/c were reported of measurements with the COSY-TOF experiment [12]. A detailed examination of the cusp was performed with data measured at a beam momentum of 3.05 GeV/c [25].

In addition to the fundamental processes which can be studied with the associated strangeness production, this elementary reaction is the basis of more complex reactions, which are under investigation and which need the precise knowledge of its observables. Among these complex reactions are the properties of hypernuclei [26], the possible existence of ppK cluster or bound states [27], and the prediction of strangeness enhancement in heavy-ion interactions as a sign for the quark gluon plasma [28]. Even information of the associated strangeness production measured at other kinematic regions can contribute to a better understanding, as they can help to describe the involved nucleon resonances and threshold effects, which have to be subtracted in order to identify these higher order effects.

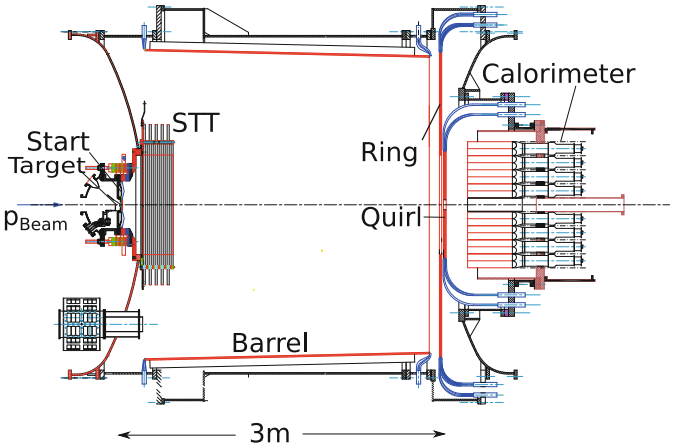

Fig. 1. Side view of the COSY-TOF spectrometer. In beam direction the start counter (Start), the straw tube tracker (STT), the barrel scintillators, the inner ring (Quirl), the outer ring (Ring), and the Calorimeter are shown. All detectors and the liquid-hydrogen target are located inside the vacuum vessel.

The purpose of this paper is to present the analysis of a high-precision measurement of the reaction $pp \rightarrow pK^+\Lambda$ in order to increase the existing data base in this momentum region by a factor of 5. Special emphasis is placed on the description of the threshold effect. Angular distributions, Dalitz plots, and invariant mass distributions are given and examined. The polarization variables will be presented in a forthcoming paper.

2 Experimental setup

The COSY-TOF experiment is a non-magnetic spectrometer, which is situated at an external beam line of the accelerator COSY in the research center Jülich. It consists of a cylindrical vacuum vessel of 3.5 m length and 3 m diameter (see fig. 1). The pressure inside the vessel is lower than 6×10^{-4} hPa.

2.1 Scintillation trigger detectors

At the inner walls of the cylinder part of the vessel 96 plastic scintillator bars are attached, which have a thickness of 15 mm, a width of ca. 10 cm and a length of 285 cm. They are arranged to form a slightly conical barrel of about 300 cm in diameter. The barrel scintillator is described in ref. [29]. The downstream end-cap of the vessel is covered by three layers of 5 mm thick plastic scintillators, which are arranged in two rings, the inner one ranging from 2.4 cm to 58 cm radius, the outer one from 54 cm to 150 cm. One of the layers is composed of 48 (inner ring) and 96 (outer ring) wedge-shaped scintillators. Each of the other two layers consists of 24 (inner ring) and 48 (outer ring) elements, formed as Archimedian spirals. The spirals change the direction of rotation from one to the other layer, therefore, 1104 (inner ring) and 2304

(outer ring) pixels can be defined by coincidences. The inner ring is described in ref. [30]. The scintillators are read out by XP2020 photo-multipliers. Downstream, the inner ring counter is followed by a scintillator calorimeter. The data of the calorimeter are not used for this measurement.

2.2 Target and beam defining detectors

The liquid-hydrogen target is located in the entrance part of the vacuum vessel. It is a cylindrical cell with a diameter of 6 mm and a length of 4 mm, which consists of $\approx 4\,\mu$m thick copper walls in the barrel part and of $0.9\,\mu$m thick Mylar window foils in the entrance and exit. In order to reduce rest gas deposition onto the target windows, the pressure surrounding the target cell is kept below 2×10^{-7} hPa. A scintillation start counter is located at a distance of about 15 mm downstream to the target center. It is made from two 1 mm thick discs, with an outer radius of 75 mm and a central beam hole of 1.5 mm radius. Each disk is divided into 12 wedge-shaped parts, which are individually read out by Hamamatsu R1450 photo-multipliers. A double-sided silicon detector disk with a thickness of $300\,\mu$m and a central beam hole of 2.75 mm radius is located 26 mm downstream. The data of this detector are only applied for $\mathrm{pK}\Sigma^+$ analysis, it will be described in a forthcoming paper on the Σ^+ results. In order to veto beam particles which hit directly the start counter, a scintillation counter with a hole of 1 mm radius is installed 50 mm upstream of the target. Further upstream at 50 cm and 100 cm two veto counters with central holes of 6 and 15 mm diameter detect beam halo particles which are around the beam core. The total beam rate and its x- and y-intensity distribution is measured with a fiber hodoscope located 1 m downstream of the spectrometer exit. The target, start and veto counters are aligned to the center of the beam line with a precision in the order of 0.1 mm with an optical telescope, which can be placed 2 m upstream of the target into the beam line. The beam is focused onto the target with a profile which has a full width at half maximum of about 1 mm. Due to precise tuning of the beam line magnets the maximum rate in the veto counters is less than 1% of the total beam rate.

2.3 Tracking detector

The main detector system is the central straw tube tracker (STT). The STT is placed about 24 cm behind the target inside the vacuum tank. It consists of 2704 straw tubes, which are arranged in 13 double layers and fixed in six orientations with an angle of 60° to each other in order to enable 3D track reconstruction. A single straw has a length of 1050 mm, 10 mm diameter and $30\,\mu$m wall thickness. The active detector volume of the 13 double layers is about 1 m in diameter and 24 cm in depth. An inner beam hole in each double layer with 15 mm diameter avoids beam interactions with the detector. Each straw tube is made of aluminized Mylar film and filled with $\mathrm{Ar} + \mathrm{CO_2}$ (80 : 20) gas mixture at a pressure of 1.2 bar. The straws are self-supporting by the over pressure of the chamber gas. Therefore, sufficient mechanical stability is provided, despite the low material budget of $X/X_0 \approx 1\%$ for 26 layers of straws. The anode is a $20\,\mu$m thick gold plated tungsten-rhenium wire which is stretched along the straw axis and held at a potential of +1820 V [31].

The arrangement of the target and detectors facilitates a volume in the z-direction from the target to the beginning of the straw detector, which is —apart from the start counter and silicon counter— free of any material. Therefore, a secondary vertex in this volume indicates with highest probability a Λ or a $\mathrm{K^0_S}$ decay.

2.4 Trigger

The trigger is defined by signals of the start counter, the barrel scintillators and the end-cap scintillators. At least one signal of the start counter and at least 4 hits in the barrel and end-cap are required. A hit in the ring counters is defined by coincident signals in two of the three layers and a hit in the barrel counter is defined by a coincidence signal of the photo-multipliers, which are situated on both ends of a barrel scintillator bar. The coincidence width is 100 ns, which takes into account the different time of flight of particles between the start and stop counters and of different light paths in the scintillators and light-guides. In order to facilitate the rate of ≈ 2000 events/s written to disk, only the STT data were read out, as this read out electronics has a dead time of $10\,\mu$s. The dead time of the ADC and TDC readout for the scintillators is in the order of $200\,\mu$s. Therefore, data which include the ADC and TDC information of the scintillators are recorded for controlling the trigger system for only about 5% of the beam time.

3 Analysis

3.1 Event reconstruction

The analysis of the $\mathrm{pK}\Lambda$ events is based on the tracking information obtained from the straw tube tracker. The determination of the correlation between drift time and the track distance to the anode is performed in two steps [32,33]: In the first step the correlation is obtained by an integration over all measured drift times and by assuming a homogeneous illumination of the straw tube by particle tracks. In the second step the position in the straw tube is calculated from reconstructed tracks, which are crossing this tube. With this information the correlation between drift time and distance to the center is recalculated. The spatial resolution of the STT is $\sigma = (140 \pm 10)\,\mu$m at 2.5 mm distance to the anode [33].

The main part of the program which extracts the tracks from the straw tube isochrones is contained in the tofStraw library [34] and described in detail in [33], [35], and [36]. The primary and decay vertices are submitted to a geometrical fit, which includes the information, that the Λ decay plane has to contain the primary vertex. The

events, for which the fit converges, are submitted to a kinematic fit by taking the geometrical fit results as start values. The kinematic fit applies momentum and energy conservation, the masses of the Λ and its decay particles are directly used as input, as the Λ is identified by the secondary vertex and the decay proton has always the smaller angle to the Λ direction. The assignment of the proton and kaon masses to the primary tracks is done by applying the kinematic fit for each of the two solutions, the result with the lower χ^2 is chosen. Events with a χ^2/NDF of less than 5, a decay length in the rest system of the Λ of larger than 2 cm and an angle of the decay proton to the Λ direction of larger than 2.5° are evaluated as pKΛ events.

3.2 Monte Carlo calculations

The corrections for the detector acceptance and the reconstruction efficiency are done with a Monte Carlo program (GEANT 3.2 [37]) with phase-space distributed events as input. The corrections were controlled with a Monte Carlo program with an input, which simulates the measured proton cm angular distribution. No significant changes of the resulting angular distributions were found. The combined acceptance and reconstruction efficiency of $pp \to pK(\Lambda \to p\pi^-)$ amounts to $(22.5 \pm 1)\%$. The primary vertex resolution is $\sigma(x, y) = (0.5 \pm 0.1)$ mm and $\sigma(z) = (1.5 \pm 0.2)$ mm. The transverse resolution of the secondary vertex is in the same range as of the primary one, while the longitudinal resolution is worse: $\sigma(z) = (2.0 \pm 0.5)$ mm. The resolution of the pΛ invariant mass is $\sigma(m_{p\Lambda}) = (1.1 \pm 0.3)\,\mathrm{MeV}/c^2$, the resolution of the KΛ and pK invariant masses are $\sigma(m_{K\Lambda}) = (1.1 \pm 0.3)\,\mathrm{MeV}/c^2$ and $\sigma(m_{pK}) = (1.0 \pm 0.3)\,\mathrm{MeV}/c^2$ [33,36].

3.3 Background

One source of background are multi-pion events. They can produce spurious secondary vertices if tracks are reconstructed erroneously. These spurious secondary vertices are expected to be close to the target, as the density of tracks is highest in this region. These background events can be identified as deviation of the measured from the calculated Λ decay length (fig. 2). The normalized data are fitted with $f(x) = p_0 \cdot \exp(-x/c\tau_0)$ in the range between 4 cm and 30 cm. p_0 is the fit coefficient and $c\tau_0$ is the literature value of the Λ decay length (7.89 cm) [38]. The background events are concentrated in the first centimeters of the decay length. The excess of the data compared to the prolongation of the fit curve between 2 cm and 4 cm adds up to 5% of the total events.

The Σ^0 background events caused by $\Sigma^0 \to \gamma\Lambda$ cannot be detected by geometry information, as the event topology is similar to the pKΛ events. The suppression of these events by the χ^2 cut of the kinematic fit is studied with a Monte Carlo sample of $pp \to pK\Sigma^0(\to \Lambda\gamma)$. The reconstruction efficiency of this sample is 8.1%, which has to be compared to the reconstruction efficiency of $pp \to pK\Lambda$ which amounts 22.5%. Including the ratio of the cross sections of 3.1 μb/21.8 μb [9] a contamination of 5% of Σ^0 events is obtained. The analysis of the Monte Carlo data of pKΣ^0 shows, that these events are shifted by the kinematic fit to the backward region of the Λ and kaon cm scattering angles. For pKΛ events this effect is not observed.

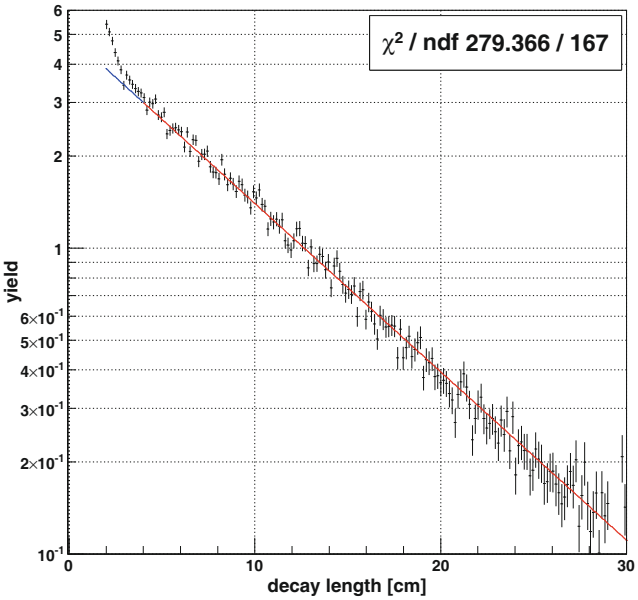

Fig. 2. Λ decay length distribution in the Λ rest system. The data are corrected for acceptance and efficiency. The fit with $p_0 \cdot \exp(-x/7.89\,\mathrm{cm})$ is applied in the range between 4 cm and 30 cm (red line). The prolongation between 2 cm and 4 cm is shown with the blue line.

4 Results

4.1 Angular distributions in the cm system

The angular distributions in the center of mass system are shown in fig. 3. The data are corrected for the detector acceptance and reconstruction efficiency and are normalized to the total cross section of 21.8 μb, which is determined in a former COSY-TOF measurement [9]. As target and projectile are identical particles, which cannot be distinguished in the cm system, these distributions have to be symmetric to $\cos\vartheta^{\mathrm{cm}} = 0$. Small deviations from symmetry are existing for all three distributions: At backward angles there is a surplus of events, which is mainly due to the $pK(\Sigma^0 \to \Lambda\gamma)$ background. At extreme forward angles ($\cos\vartheta^{\mathrm{cm}} \geq 0.95$) of the proton and kaon distributions a deficit of events is found. The affected range corresponds to scattering angles in the lab system of smaller than 5°–6° degrees. It is supposed that the deficit of events is caused by an efficiency drop in the cones of the start counter, which cannot be exactly described by the Monte Carlo program.

While the angular distribution of the heavier reaction products, p and Λ, exhibit distinct deviations from uniformity, the distribution of the lighter kaon is nearly constant. This behavior is examined in detail in sect. 5.1.

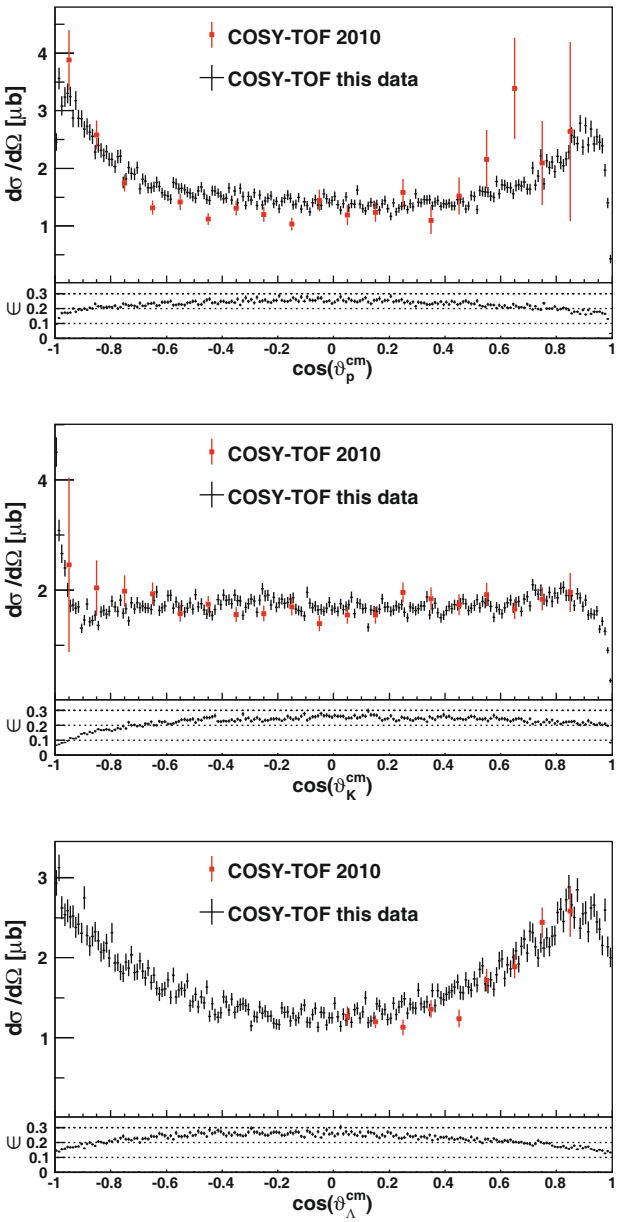

Fig. 3. The angular distributions in the cm system are shown for the proton (upper figure), kaon (middle), and Λ (bottom). The results from a former COSY-TOF measurement [9] are given as red squares. Beneath each distribution the detector acceptance and reconstruction efficiency ϵ is shown.

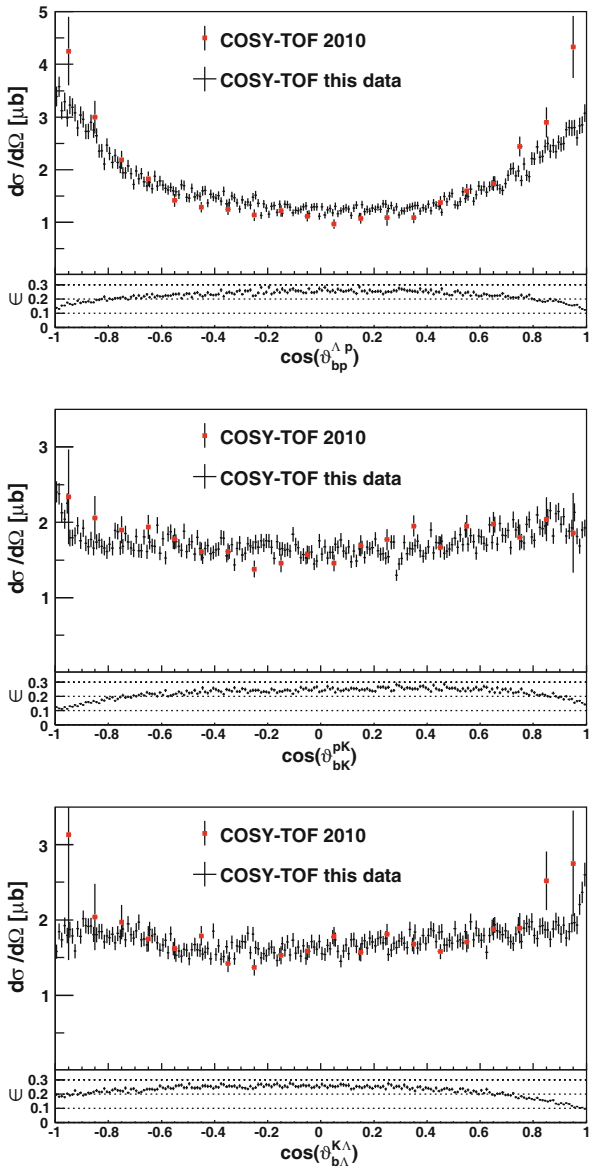

Fig. 4. The angular distribution in the pΛ Gottfried-Jackson frame is shown in the upper figure. Middle: pK Gottfried-Jackson frame, bottom: KΛ Gottfried-Jackson frame. The results from a former COSY-TOF measurement [9] are given as red squares. Beneath each distribution the detector acceptance and reconstruction efficiency ϵ is shown.

4.2 Gottfried-Jackson angular distributions

The angular distributions in the three two-particle subsystems of the final state pKΛ are constructed by boosting the momenta into the rest system of the two particle system. The angle between the boosted beam vector and one of the particles of the two particle system is the Gottfried-Jackson (GJ) angle. It is denoted with $\vartheta^{\mathrm{ij}}_{\mathrm{bi}}$, where i, j are the particles of the two particle rest system and b stands for the boosted-beam direction. The GJ angular distributions are shown for the rest systems of Λp, pK, and KΛ in fig. 4. In contrast to the cm distributions the GJ angular distributions do not have to be symmetric to $\cos\vartheta^{\mathrm{ij}}_{\mathrm{bi}} = 0$.

While only in the KΛ rest system higher angular momenta due to nucleon resonances are expected, the GJ angular distributions exhibit the highest anisotropy for the Λp rest system. The GJ angular distributions are examined in dependence on bins of the invariant masses in sect. 5.2.2.

4.3 Dalitz plots

The Dalitz plots are normalized by scaling the maximum channel content to 1. The Dalitz plot of $m^2_{\mathrm{p}\Lambda}$ *versus* $m^2_{\mathrm{K}\Lambda}$

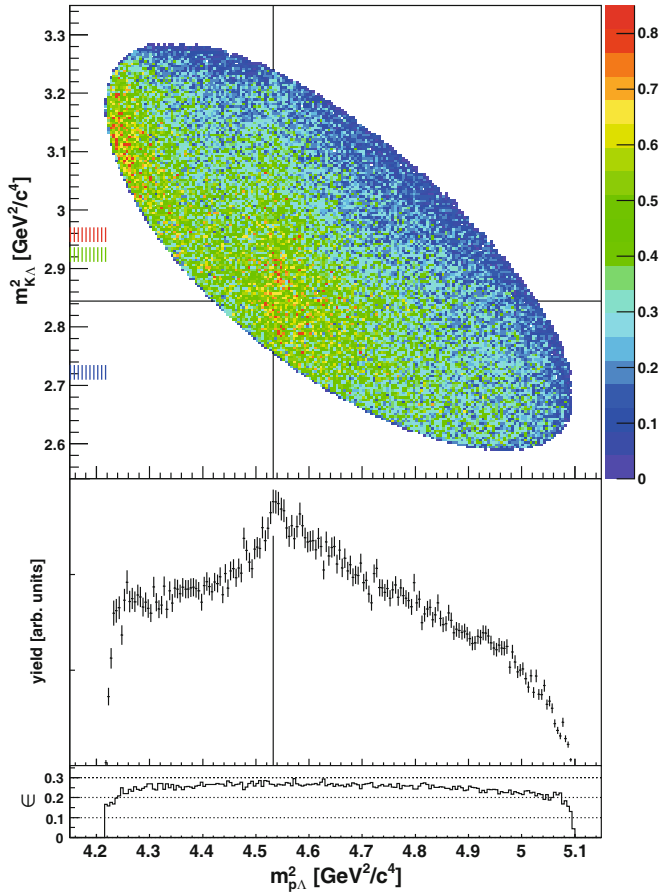

Fig. 5. Top: The Dalitz plot of the measured data. In order to enhance the visibility of the structures the color code is truncated to 0.85 (less than 0.1% of the bins have an occupancy of larger than 0.85). The black horizontal line indicates the KΣ threshold, the vertical one the NΣ threshold. The red area at the ordinate indicates the mass of the N*(1720) resonance, the green area indicates the N*(1710) resonance, and the blue area the N*(1650) resonance. Middle: The projection on the squared invariant mass pΛ is shown. This projection is corrected by the combined detector and reconstruction efficiency, which is shown in the bottom frame. The NΣ threshold is indicated by the black line.

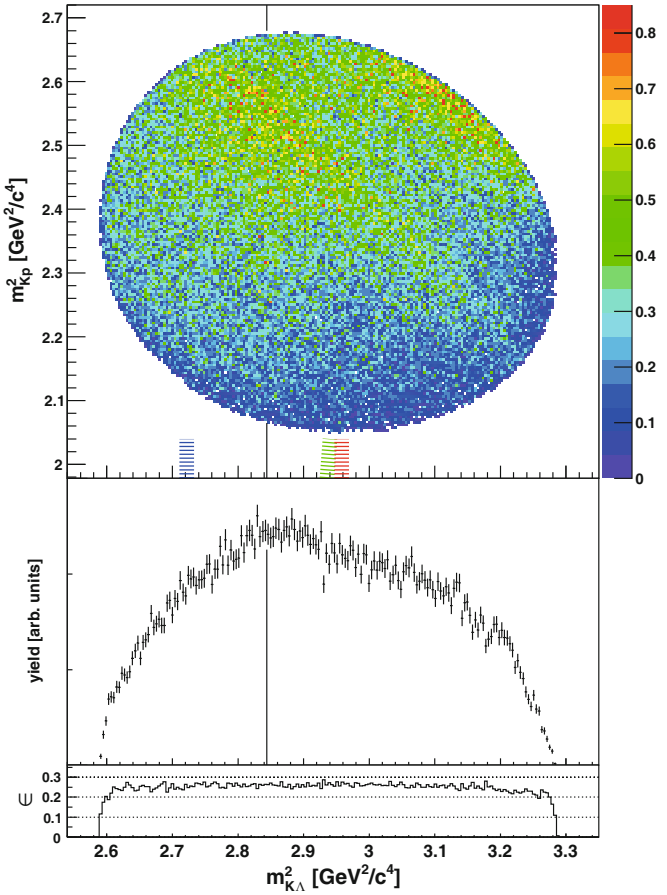

Fig. 6. Top: The Dalitz plot of the measured data. In order to enhance the visibility of the structures the color code is truncated to 0.85 (less than 0.1% of the bins have an occupancy of larger than 0.85). The black vertical line indicates the KΣ threshold. The red area at the abscissa indicates the mass of the N*(1720) resonance, the green area indicates the N*(1710) resonance, and the blue area the N*(1650) resonance. Middle: The projection on the squared invariant mass KΛ is shown. This projection is corrected by the combined detector and reconstruction efficiency, which is shown in the bottom frame. The KΣ threshold is indicated by the black line.

is shown in fig. 5. Two dominant structures, which are stretched mainly in the vertical direction, are observed. The first one is located at low pΛ invariant masses and arises from the pΛ final-state interaction [3]. The second structure located at the NΣ threshold has its maximum intensity around $m^2_{\mathrm{K}\Lambda} \approx 2.85\,\mathrm{GeV}^2/c^4$ and extenuates with rising KΛ invariant mass.

The Dalitz plot of $m^2_{\mathrm{K}\Lambda}$ *versus* m^2_{Kp} is shown in fig. 6. The two dominant structures of the previous Dalitz plot are emerging as diagonal spread elevations. Again the structure connected to the NΣ threshold exhibits a strong intensity variation across the Dalitz plot.

No structures at the KΣ threshold or near the resonance masses can be detected. A detailed analysis of the invariant mass distributions is given in sect. 5.2.

5 Detailed examinations and discussions

5.1 CM angular distributions

Former COSY-TOF measurements exhibit that the $l = 2$ Legendre polynomial coefficient, which is a measure for the contribution of higher partial waves, rises with increasing beam momentum [9]. The data presented here allow for the first time to extract the Legendre coefficients not only from the integrated angular distribution but from a series of angular distributions, each constructed for a bounded range of the center-of-mass momentum.

For all reaction particles (p, K, Λ) the magnitude of the center-of-mass momentum of the particle is divided into 6 equidistant intervals. For each momentum interval the angular distribution of the particle has been fit according

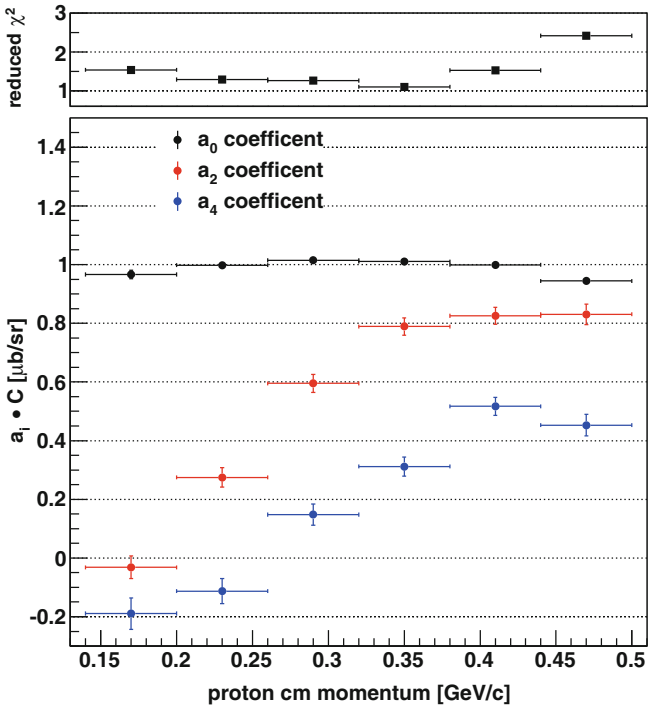

Fig. 7. The dependence of the fit coefficients of the proton angular distribution on the proton center-of-mass momentum is shown. The upper small figure shows the corresponding reduced χ^2 of the fit.

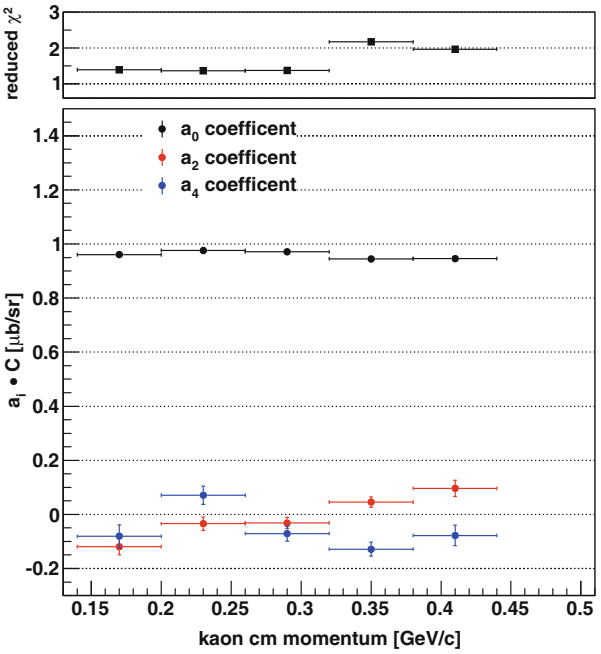

Fig. 8. The dependence of the fit coefficients of the kaon angular distribution on the kaon center-of-mass momentum is shown. The last bin is missing, as the maximum kaon momentum is less than 0.44 GeV/c. The upper small figure shows the corresponding reduced χ^2 of the fit.

to the formula

$$\frac{\mathrm{d}\sigma}{\mathrm{d}\cos\vartheta^{\mathrm{cm}}} = C \cdot (a_0 P_0 + a_2 P_2(\cos\vartheta^{\mathrm{cm}}) + a_4 P_4(\cos\vartheta^{\mathrm{cm}})), \quad (1)$$

where C is a normalization constant. This formula describes the differential cross section directly as a sum of Legendre polynomials P_i by neglecting the interference terms. Due to identical particles in the initial state, the angular distributions in the center-of-mass system have to be symmetric with respect to $\cos\vartheta^{\mathrm{cm}} = 0$. Therefore, the coefficients a_1 and a_3 are set to zero. With this parametrization and the restriction to the maximum angular momentum of $l = 2$, the coefficient a_2 contains products of SD, PP, and DD partial wave amplitudes, and a_4 contains only the DD partial wave product. The angular distributions are normalized for each range of the center-of-mass momentum separately, in order to be independent of the variation of the cross section with the center-of-mass momentum.

The angular distributions are shown in the appendix (fig. 19 for the proton, fig. 20 for the kaon and fig. 21 for the Λ particle). In addition, in each figure the Legendre polynomials P_0, P_2, and P_4, weighted with the corresponding fit coefficients, are plotted and the corresponding momentum range is indicated. For the proton and kaon the fit is restricted to the range of $-0.95 \leq \cos\vartheta^{\mathrm{cm}} \leq 0.95$. The limit in the backward direction takes into account the increase of background at this region. The cut in the forward range corresponds to a limit in the laboratory scattering angle of about 5°, and takes into account that the proton and kaon have to be detected by the start-counter, of which the efficiency determination for the very small angles has a larger error compared to other angles.

The variations of the coefficients a_0, a_2, and a_4 with the center of mass momentum are shown in figs. 7, 8, 9 for p, K, and Λ, respectively. The coefficient a_2 of the proton rises nearly linearly from 0.15 GeV/c to 0.35 GeV/c and is constant in the momentum region 0.35–0.5 GeV/c. In contrast to this behavior the coefficient a_2 of the Λ rises with the third power of the cm momentum:

$$a_2 = 1/C \cdot f \cdot (p_\Lambda^{\mathrm{cm}}[\mathrm{GeV}/c])^3,$$

with $f = (12.2 \pm 1.4)\,\mu\mathrm{b}/(\mathrm{GeV}/c)^3$ (see red line in fig. 9). C is the normalization factor defined in eq. (1).

The coefficient a_4 of the proton starts to be significantly different from 0 at the cm momentum of 0.3 GeV/c and rises up to $1/C \cdot 0.6\,[\mu\mathrm{b/sr}]$ at 0.45–0.5 GeV/c. The fit of the Λ distribution gives only for the momentum bin of 0.5 GeV/c a significant a_4 contribution with about 1/3 compared to the proton angular distribution. The kaon angular distribution can be described for all momentum bins by the coefficient a_0 alone, no higher Legendre polynomials are needed for the fit. The reduced χ^2 of the fit increases only by a factor of 1.1 to 1.3 by omitting the P_2 and P_4 polynomials in the fitting procedure.

The isotropy of the kaon angular distribution, even for the highest momenta, is in contrast to the behavior of the ω in the pp → ppω reaction [39]. Here the cm angular distribution of the lighter particle (ω) is strongly anisotropic (for the measurement with a beam momentum of

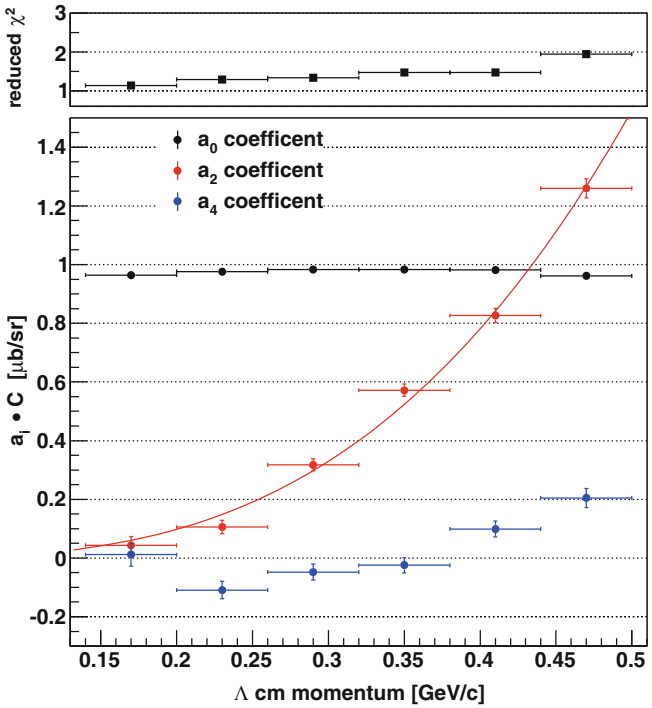

Fig. 9. The dependence of the fit coefficients of the Λ angular distribution on the Λ center-of-mass momentum is shown. The upper small figure shows the corresponding reduced χ^2 of the fit. The distribution of the coefficient a_2 is fitted with $c \cdot x^3$ (continuous red line).

3.059 GeV/c the maximum cm momentum of the ω is with 0.4 GeV/c approximately in the same range of the maximum cm momentum of the kaon). The protons exhibit a nearly flat angular distribution in contrast to the proton or Λ of the pKΛ reaction. A better comparison is the pp $\rightarrow$ ppη reaction, as the mass of the η, compared to the one of the ω, is closer to the kaon mass. Data measured at a beam momentum of 2.94 GeV/c, where the η has 0.554 GeV/c cm momentum, yield a strongly anisotropic angular distribution. In contrast, the angular distribution is isotropic at a beam momentum of 3.67 GeV/c, corresponding to η cm momentum of 0.774 GeV/c [40]. Therefore, there is no clear sign, whether the cm angular distribution of the lightest particle of a three-particle system is particularly isotropic due to kinematical effects.

5.2 Invariant mass distributions

For better comparability with literature —especially concerning the threshold examinations— the linear invariant mass distributions are analyzed.

The measured invariant mass distribution is given by

$$\frac{\mathrm{d}\sigma^{\mathrm{meas}}}{\mathrm{d}m_{\mathrm{ij}}} = \mathrm{PS}(m_{\mathrm{ij}}) \cdot |\mathrm{M}(m_{\mathrm{ij}})|^2 \cdot \epsilon(m_{\mathrm{ij}}), \qquad (2)$$

PS denotes the phase-space volume, $\mathrm{M}(m_{\mathrm{ij}})$ the reaction amplitude, and ϵ is the detector acceptance and reconstruction efficiency, which are dependent on the invariant mass. By modeling the reaction with the Monte Carlo technique the phase-space, the acceptance and reconstruction efficiency are calculated:

$$\frac{\mathrm{d}\sigma^{\mathrm{MC}}}{\mathrm{d}m_{\mathrm{ij}}} = \mathrm{PS}(m_{\mathrm{ij}}) \cdot \epsilon(m_{\mathrm{ij}}). \qquad (3)$$

The division of the measured distribution by the Monte Carlo distribution generates a spectrum, which is only dependent on the reaction amplitude $\mathrm{M}(m_{\mathrm{ij}})$ and no assumptions on the normalization to the phase-space distribution are needed[1]. In the following these spectra are analyzed.

5.2.1 Proton-Λ invariant mass

The main goal of the examination of this invariant mass distribution is the analysis of the behavior at the NΣ threshold. In the strict sense there are two thresholds: nΣ^+ at 2.129 GeV/c^2 and pΣ^0 at 2.131 GeV/c^2. This mass difference is about 1σ of the invariant mass resolution and not resolved in the data. In the following calculations the mass of the lower threshold is used, as this channel dominates the cusp effect [42]. For convenience the threshold is named NΣ threshold.

In order to examine the NΣ threshold we assume as a working hypothesis that the final state interaction (FSI), the NΣ threshold (TH), and the reflections of N* resonances (RF) are independent and interference terms are negligible:

$$\frac{\mathrm{d}\sigma^{\mathrm{meas}}}{\mathrm{d}m_{\mathrm{p}\Lambda}} \Big/ \frac{\mathrm{d}\sigma^{\mathrm{MC}}}{\mathrm{d}m_{\mathrm{p}\Lambda}} = \mathrm{FSI}(m_{\mathrm{p}\Lambda}) + \mathrm{TH}(m_{\mathrm{p}\Lambda}) + \mathrm{RF}(m_{\mathrm{p}\Lambda}). \qquad (4)$$

Of course this is a simplification, as the reflections of the N* resonances can interfere with the final-state interaction and the threshold effect. The final-state interaction, the reflection of N* resonances and the threshold effect are described with functions with free parameters. The parameters are determined by fitting the invariant mass distribution with the sum of these functions.

The final-state interaction is treated like the other terms as an additive term in order to incorporate that the FSI has strong influence at low pΛ invariant mass and this influence is negligible towards larger invariant masses[2]. This is in contrast to the ansatz, where the reaction amplitude is factorized with the FSI amplitude (see for instance [3] and references therein).

The final-state interaction is parameterized with

$$\mathrm{FSI}(m_{\mathrm{p}\Lambda}) = \exp\left(c_0 + \frac{c_1}{m^2_{\mathrm{p}\Lambda} - c_2}\right). \qquad (5)$$

[1] In publications of the DISTO Collaboration (*e.g.*, [41]) this distribution is named "deviation spectrum".

[2] A similar behavior is measured for the pp final state in $pp \rightarrow pp\eta$ at an excess energy of 41 MeV [43] and in $np \rightarrow pp\pi^-$ at excess energies between 405 and 465 MeV [44].

The effective scattering length can be expressed by two of the three coefficients of eq. (5):

$$a_{\text{eff}} = -1/2\,\hbar c\, c_1 \sqrt{\frac{m_{\text{min}}^2}{m_{\text{p}} m_{\Lambda}} \cdot \frac{m_{\text{max}}^2 - m_{\text{min}}^2}{(m_{\text{max}}^2 - c_2) \cdot (m_{\text{min}}^2 - c_2)^3}}\,, \quad (6)$$

m_{min} and m_{max} denote the range of the invariant mass $m_{\text{p}\Lambda}$ in which this formula is applied to determine the scattering length. Equations (5) and (6) are given in [35], they are derived in [16]. Equation (6) is applied to express the coefficient c_1 with the effective scattering length. The value of $a_{\text{eff}} = 1.233\,\text{fm}$ is taken, which is deduced from data measured at a beam momentum of $2.7\,\text{GeV}/c$ [35]. At this beam momentum no disturbing effects of the NΣ threshold are present. The influence of the N* resonances were tested by evaluating different regions of the Dalitz plot, they give limits of the measured effective scattering length between -1.4 and $-1.2\,\text{fm}$ [35], at the beam momentum of 2.95 these limits were found to be larger with -0.9 and $-2.1\,\text{fm}$ [18]. With this procedure the final state interaction at $2.95\,\text{GeV}/c$ is expressed with two parameters c_0 and c_2.

The nucleon resonances N*(1650), N*(1710), N*(1720) contribute to deviations from the phase-space in the Dalitz plot [8]. As these resonances decay into $\text{K}^+\Lambda$ their influence can be seen directly in the invariant mass distribution of $m_{\text{K}^+\Lambda}$ and as reflections in the invariant mass distribution of $m_{\text{p}\Lambda}$. As their widths are in the range of 50–400 MeV [38] the reflections are slowly varying with $m_{\text{p}\Lambda}$ compared to the FSI and the threshold effect, whose structures are smaller than $20\,\text{MeV}/c^2$. Therefore, these reflections are parameterized as a polynomial of second order. The main purpose of this parametrization is to quantify the background beneath the cusp effect, and not to draw conclusions on these resonances. For simplicity this part is named "reflections" in the further description.

As the threshold effect is expected to be a coupled channel effect, we apply the Flatté formalism [45]. This formalism was developed to describe the $\eta\pi$ ($\pi\pi$) interaction at the two-kaon threshold. It is assumed that the $a_0(980)$ ($f_0(980)$) resonance changes its width due to the opening channel of KK thus inducing a cusp structure. This formalism is adapted to the pΛ channel by assuming a virtual state of pΛ, which decays into pΛ and into NΣ, thus causing a cusp effect [25].

$$\text{TH}(m_{\text{p}\Lambda}) = C \left| \frac{m_{\text{r}} \sqrt{\Gamma_0 \cdot \Gamma_{\Lambda\text{p}}}}{m_{\text{r}}^2 - m_{\Lambda\text{p}}^2 - i m_{\text{r}} (\Gamma_{\Lambda\text{p}} + \Gamma_{\Sigma\text{N}})} \right|^2, \quad (7)$$

m_{r} and Γ_0 are the mass and the total width of a virtual pΛ state. C is a normalization parameter. As it cannot be separated from the unknown total width Γ_0, the product $C \cdot \Gamma_0$ is treated as one parameter for the fitting procedure. $\Gamma_{\Lambda\text{p}}$ and $\Gamma_{\Sigma\text{N}}$ are the partial decay widths of the virtual state, which are given by

$$\Gamma_{\Lambda\text{p}} = g_{\Lambda\text{p}} \cdot q_{\Lambda\text{p}} \quad (8)$$

and

$$\Gamma_{\Sigma\text{N}} = g_{\Sigma\text{N}} \cdot q_{\Sigma\text{N}},$$

$g_{\Lambda\text{p}}$ and $g_{\Sigma\text{N}}$ are the coupling constants of the two channels to the virtual pΛ state and $q_{\Lambda\text{p}}$ and $q_{\Sigma\text{N}}$ are the cm momenta in the corresponding two-body subsystems. In dependence on the invariant mass $m_{\text{p}\Lambda}$, $q_{\Sigma\text{N}}$ is imaginary below the NΣ threshold,

$$q_{\Sigma\text{N}} = i \frac{\sqrt{((m_{\Sigma^+} + m_{\text{n}})^2 - m_{\text{p}\Lambda}^2) \cdot (m_{\text{p}\Lambda}^2 - (m_{\Sigma^+} - m_{\text{n}})^2)}}{2 m_{\text{p}\Lambda}}\,, \quad (9)$$

and real above the NΣ threshold,

$$q_{\Sigma\text{N}} = \frac{\sqrt{(m_{\text{p}\Lambda}^2 - (m_{\Sigma^+} + m_{\text{n}})^2) \cdot (m_{\text{p}\Lambda}^2 - (m_{\Sigma^+} - m_{\text{n}})^2)}}{2 m_{\text{p}\Lambda}}\,. \quad (10)$$

The cm momentum $q_{\Lambda\text{p}}$ is always real and given by exchanging the Σ^+ and neutron mass (m_{Σ^+}, m_{n}) with the Λ and proton mass (m_{Λ}, m_{p}) in eq. (10). A detailed examination of Flatté-like distributions [46] reveals that the coupling constants and the mass of the virtual state show a scaling behavior. Therefore, the coupling constant $g_{\Lambda\text{p}}$ is fixed to the arbitrarily chosen value of 1, and only the remaining parameters $C\Gamma_0$, $g_{\Sigma\text{N}}$, and m_{r} are determined together with the parameters for the reflections and FSI by a fit procedure.

The measured invariant mass distribution —divided by the Monte Carlo distribution— fitted with the function as described in eq. (4) is shown in fig. 10. The fit starts at the kinematic limit of $m_{\text{p}} + m_{\Lambda}$ and is limited to $2.250\,\text{GeV}/c^2$, which is $8\,\text{MeV}/c^2$ below the maximum possible kinematical value. This limit is chosen as the data and Monte Carlo distributions have above this value a sharp decrease to zero, therefore, the uncertainties of the ratios are large.

The structures of the data are well described by the fit. The sharp rising leading edge, the peak at the threshold, and the slow decreasing above the threshold is reproduced by the Flatté formalism. The mass of the virtual pΛ state is $2.31\,\text{GeV}/c^2$. However, this value is depending on the arbitrarily chosen value of the pΛ coupling constant to this virtual state. Changing this coupling constant for instance from 1 to 0.5 produces a fit result for the mass of the virtual pΛ state of $2.20\,\text{GeV}/c^2$. As remarked in [45], the mass of the virtual state has to be larger than the threshold in order to generate a sharp cusp shape. For masses below the threshold, the distribution varies more smoothly, and is more similar to a Breit-Wigner distribution. The coupling constant of the virtual state to the NΣ channel ($g_{\Sigma\text{N}} = 1.253 \pm 0.189$) is larger than the coupling constant to the pΛ ($g_{\Lambda\text{p}} = 1$, fixed value) channel. This is in contrast to the previous analysis [25], which applied

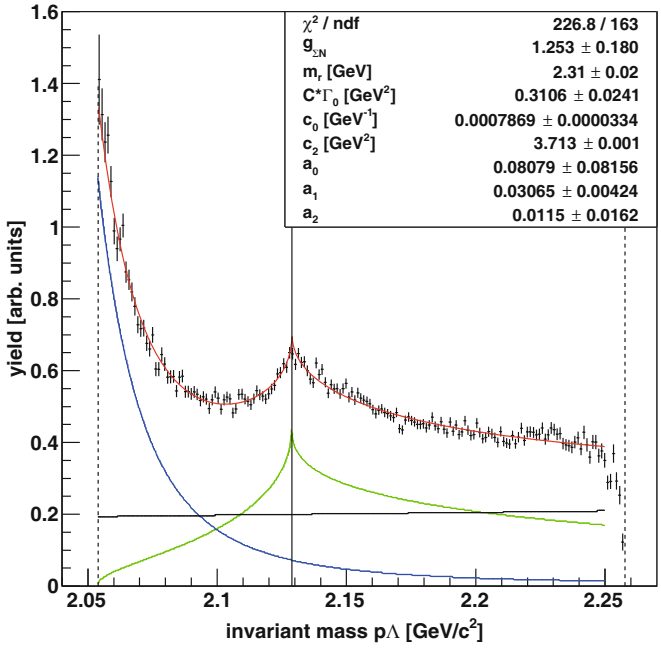

Fig. 10. The whole data set divided by the Monte Carlo data is shown as dots with error bars. The fit result is given by the red line, it is composed of the FSI part (blue line), the part of the reflections (black line), and the Flatté distribution (green line). The NΣ threshold is marked with the vertical black line. The kinematic limits are indicated by two dashed lines.

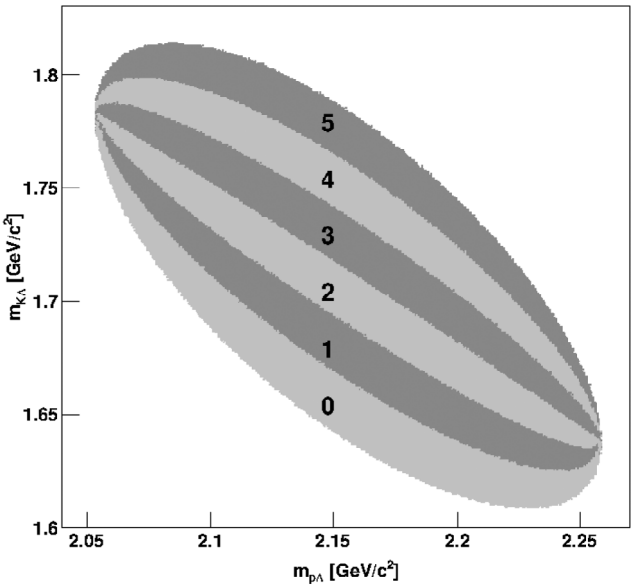

Fig. 11. The division of the Dalitz plot into six slices by selecting ranges of the helicity angle between proton and kaon in the pΛ subsystem is shown. If the Dalitz plot is filled according to the phase-space, the projection of the slices $i = 0 \ldots 5$ onto the invariant mass pΛ results in identical distributions.

a different mass of the virtual state. The first attempt to describe the threshold behavior of the pΛ invariant mass distribution with the Flatté formula was performed in [21], where a measurement of $K^- d \to p\Lambda\pi^-$ is described. Here

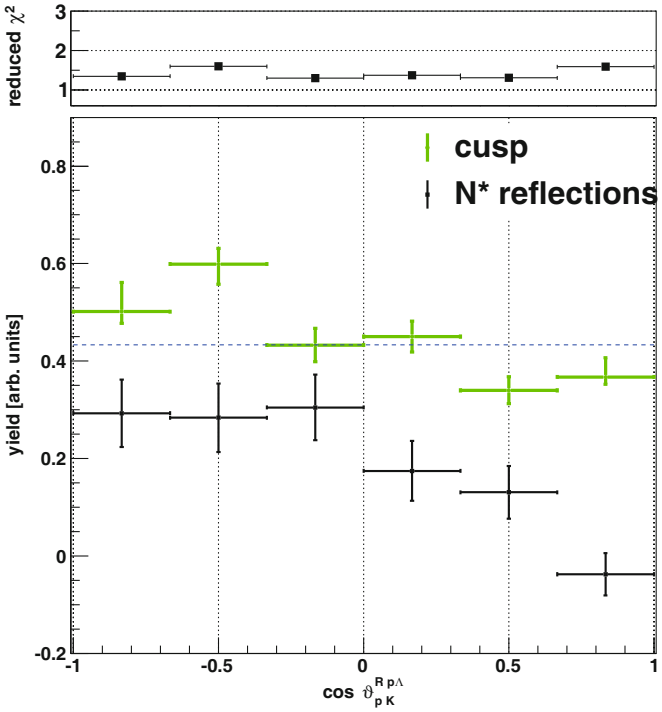

Fig. 12. The height of the cusp (green crosses) and the amount of the reflections at the cusp position (black crosses) for the different regions of the Dalitz plot as shown in fig. 11. The blue dashed line shows the fit result of the height of the cusp of the total data set. As the errors of the fit parameter $C\Gamma_0$ are found to be asymmetric, the errors of the MIGRAD routine of the ROOT [47] program are shown. The upper small figure shows the corresponding reduced χ^2 of the fit.

the best-fit result is obtained with a mass of $2.20\,\mathrm{GeV}/c^2$ as input parameter.

As can be seen in the Dalitz plot of fig. 5, the density in the NΣ threshold region, is strongly decreasing with increasing $m_{K\Lambda}$. In order to examine, whether this variation is due to the cusp effect or due to the N* contributions, the Dalitz plot is divided into 6 slices, by applying cuts on the helicity angle between the proton and the kaon in the pΛ subsystem (see fig. 11). The limits of each slice are given by

$$-1 + i \cdot 1/3 < \cos\vartheta_{\mathrm{pK}}^{\mathrm{Rp}\Lambda} < -1 + (i+1) \cdot 1/3, \qquad (11)$$

with $i = 0 \ldots 5$. The projection of these slices onto the pΛ invariant mass results in identical distributions if the Dalitz plot is filled according to phase-space.

For each slice the invariant mass pΛ is fitted with the same function as applied for the whole data set. As the FSI distribution is expected to be independent of the helicity angle, the parameters c_0, c_2 are fixed to the values which are obtained by the fit of the whole data set. In addition it is assumed that the cusp does not change its shape, therefore, the parameters m_r, and $g_{N\Sigma}$ are fixed to the values obtained by the whole data fit. $C\Gamma_0$ and the coefficients of the reflections are determined for each slice with the same fit procedure. The height of the cusp

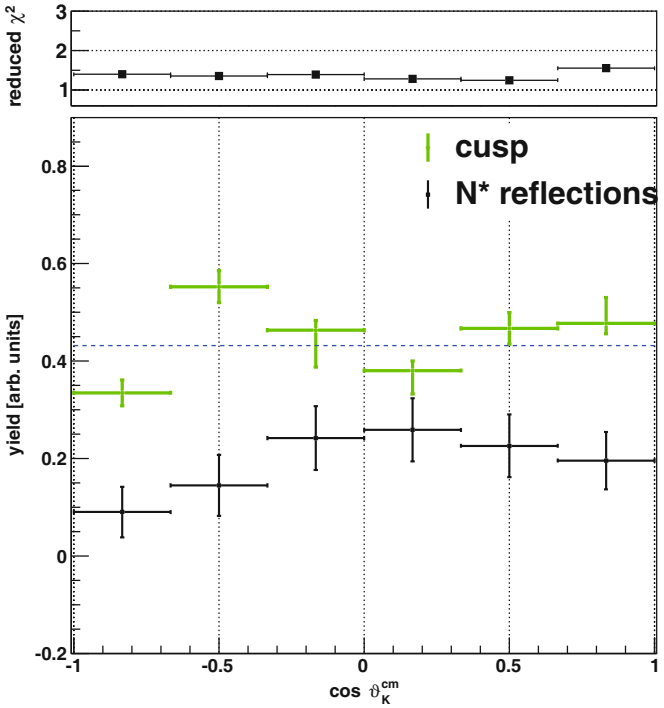

Fig. 13. The height of the cusp (green crosses) and the amount of the reflections at the cusp position (black crosses) for the different regions of $\cos\vartheta_K^{cm}$. The blue dashed line shows the fit result of the height of the cusp of the total data set. As the errors of the fit parameter $C\Gamma_0$ are found to be asymmetric, the errors of the MIGRAD routine of the ROOT [47] program are shown. The upper small figure shows the corresponding reduced χ^2 of the fit.

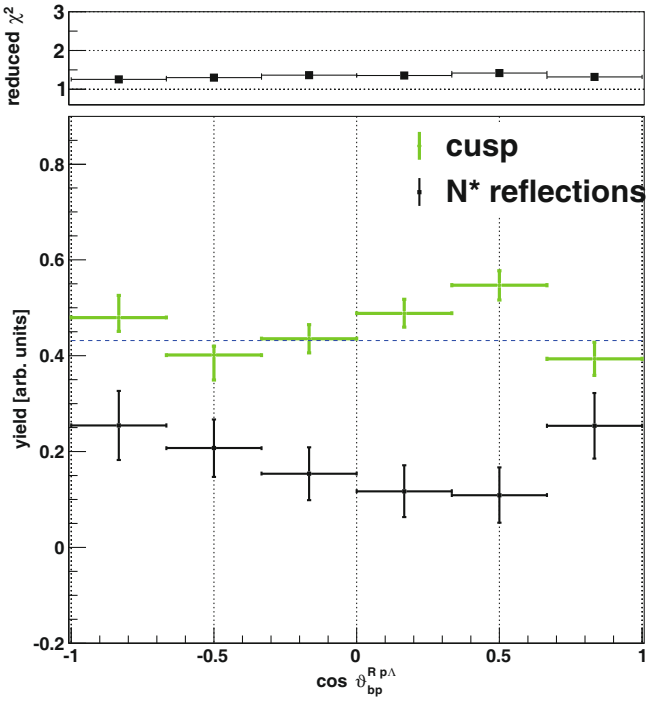

Fig. 14. The height of the cusp (green crosses) and the amount of the reflections at the cusp position (black crosses) for the different regions of $\cos\vartheta_{bp}^{Rp\Lambda}$. The blue dashed line shows the fit result of the height of the cusp of the total data set. As the errors of the fit parameter $C\Gamma_0$ are found to be asymmetric, the errors of the MIGRAD routine of the ROOT [47] program are shown. The upper small figure shows the corresponding reduced χ^2 of the fit.

is proportional to $C\Gamma_0$. With $m_r = 2.31\,\mathrm{GeV}/c^2$ the proportional factor is 1.39. As the shape of the cusp is constant, $C\Gamma_0$ is in addition proportional to the area beneath the cusp described by the Flatté function. The amount of the reflections beneath the cusp is determined as the value of the second order polynomial at the cusp position ($m_{p\Lambda} = 2.129\,\mathrm{GeV}/c^2$). The individual distributions of the slices and their fit results are shown in the appendix (fig. 22). The variation of the height of the Flatté distribution and the amount of the reflections at the threshold is shown in fig. 12. While the height of the Flatté distribution varies only slowly with the helicity angle, the part of the reflections is nearly constant for the first three slices and then drops from 0.3 to 0 in the last three slices. This indicates that the large intensity variation in the Dalitz plot along the cusp line is caused by the background generated by the N* resonances.

The assumption, that the cusp does not change the shape, seems to be justified by the fit results. It can be seen in the appendix (fig. 22), that the cusp is well described by the fit function, having the same parameters, which affect the cusp shape. The quality of the fit is nearly the same for each slice, all reduced χ^2 are in the range of 1.4 ± 0.2.

The angular distribution of the cusp effect reflects the angular distribution of the pΛ system, which stems from the NΣ system at the threshold. The angular momenta between p and Λ inside the pΛ system are described by the Gottfried-Jackson angular distribution ($\cos\vartheta_{pb}^{Rp\Lambda}$). As the p$\Lambda$ system has the same spin-parity as the NΣ system at the threshold ($J^P = 0^+, 1^+$), it can only be in relative S or D waves [25]. The angular momentum of the cusp can be examined with the kaon angular distribution in the cm system, which is one of the two particle subsystem K-(NΣ) and thus the kaon angular distribution is the mirrored one of (NΣ). This angular distribution has to be symmetric to $\cos\vartheta_K^{cm} = 0$. Both angular distributions $\cos\vartheta_K^{cm}$ and $\cos\vartheta_{pb}^{Rp\Lambda}$ of the height of the Flatté distribution and the amount of the reflections beneath the cusp are generated with the slice method as described in the previous section. In this case $\cos\vartheta_K^{cm}$ and $\cos\vartheta_{pb}^{Rp\Lambda}$ are divided into 6 bins. The fit results for the $\cos\vartheta_K^{cm}$ slices are shown in fig. 23 and for the $\cos\vartheta_{pb}^{Rp\Lambda}$ slice in fig. 24 in the appendix.

The variation of the height of the Flatté distribution and the amount of the reflections at the threshold in dependence on the different slices is shown in figs. 13, 14.

No systematic deviations of the cusp height distributions from isotropy, which could be a hint for P or D waves, can be seen. This is a confirmation of the findings in [25], which are based on a different data set of COSY-TOF and on a different analysis method. The shape of the cusp does not change with the examined angles, as can be seen

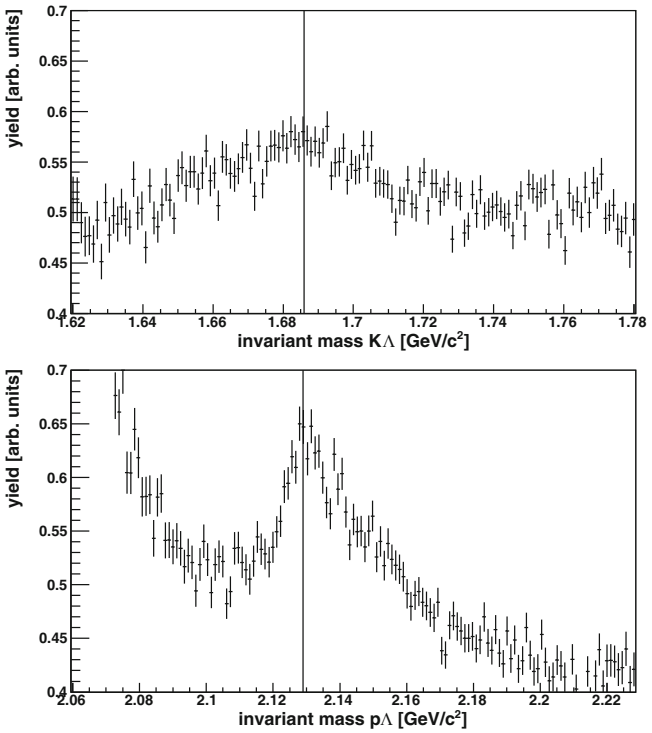

Fig. 15. The KΣ threshold region of the KΛ invariant mass is shown (top) in comparison to the NΣ threshold region of the pΛ invariant mass (bottom). The thresholds are indicated by the vertical lines. In contrast to the strong and sharp enhancement at the NΣ threshold in the lower figure, no sharp structure is seen at the KΣ threshold in the upper figure.

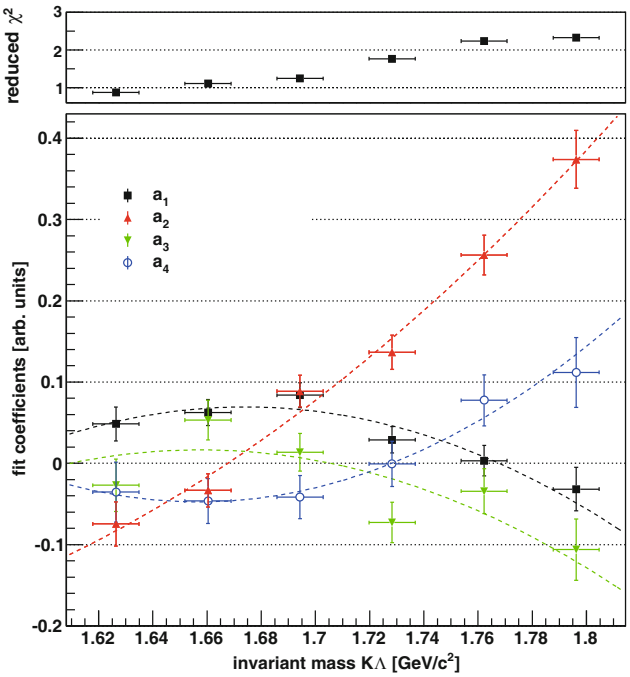

Fig. 16. Fit results of the coefficients of eq. (12) obtained from the GJ angular distributions $\cos\vartheta^{\mathrm{RK}\Lambda}_{\mathrm{b}\Lambda}$ for six bins of the KΛ invariant mass with equal widths (lower figure). The coefficient a_0 is close to 1, it is given in fig. 25. The upper figure shows the corresponding reduced χ^2 of the fit. The dashed lines are generated with a second degree polynomial fit and have the only purpose to guide the eye.

from the fits of the individual slices. The reduced χ^2 of all fits does not deviate from the mean value of 1.36 by more than 0.2.

5.2.2 Kaon-Λ invariant mass

Deviations of the KΛ invariant mass from phase-space can be caused by a KΣ threshold effect or by nucleon resonances, which decay into the KΛ channel. In addition reflections of the FSI and the NΣ cusp in the pΛ invariant mass distributions contribute to the deviations.

At the KΣ threshold no cusp-like structure is detected, as shown in fig. 15. Here the KΣ threshold region is compared to the NΣ threshold region. The effect of the pΣ cusp is estimated to be $(15 \pm 5)\%$ of the total cross section, which corresponds to $(3 \pm 1)\,\mu$b. From fig. 15 it can be seen that the height of the NΣ cusp compared to the error bars of the measurement is about 10/1, therefore, the upper limit of a possible KΣ cusp —if it has a similar shape as the NΣ cusp— is in the order of $0.3\,\mu$b.

The contribution of N* resonances decaying into KΛ will vary with the distance of the invariant mass KΛ to the resonance mass. As N* resonances affect the composition of the angular momenta, this composition is tested for different ranges of the invariant mass KΛ. The angular distribution for the KΛ rest system given by the cosine of the Gottfried-Jackson angle $\vartheta^{\mathrm{RK}\Lambda}_{\mathrm{b}\Lambda}$ is generated for six ranges of the KΛ invariant mass. The distributions and the corresponding ranges are shown in the appendix in fig. 25. The angular distributions are fitted with a formula describing the differential cross section as a sum of Legendre polynomials by neglecting the interference terms. As the angular distributions do not have to be symmetric to $\cos\vartheta = 0$ —as is the case of the center-of-mass system— the odd terms of the Legendre polynomials have to be included,

$$\frac{\mathrm{d}\sigma}{\mathrm{d}\cos\vartheta^{\mathrm{RK}\Lambda}_{\mathrm{b}\Lambda}} = C \cdot \sum_{i=0}^{n} \left(a_i P_i\left(\cos\vartheta^{\mathrm{RK}\Lambda}_{\mathrm{b}\Lambda}\right)\right), \qquad (12)$$

C is a normalization constant, for these fits the highest order $n = 4$ is chosen. The dependence of the Legendre coefficients a_i on the KΛ invariant mass slices is shown in fig. 16.

As the KΛ invariant mass is proportional to the K and Λ cm momentum the rising momenta of the KΛ invariant mass slices in addition influences the angular distributions, as is shown in sect. 5.1 for the cm angular distributions. Therefore, an influence of N* resonances on the variation of the fit coefficients $a_0 \ldots a_4$ with the invariant mass can only be visible in the comparison with the corresponding fit coefficients calculated in the same manner for the invariant masses of pK and pΛ, where no resonances are expected. The GJ angular distributions for these invariant masses are shown in the appendix (figs. 26, 27) and the variation of the coefficients in figs. 17, 18.

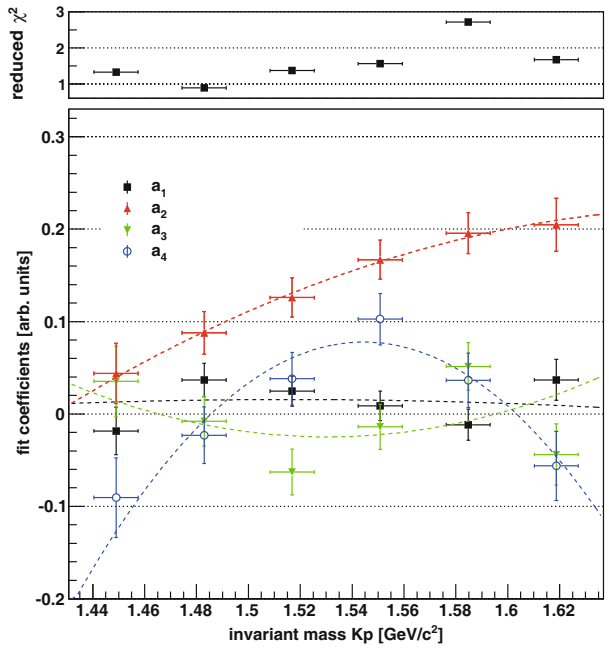

Fig. 17. Fit results of the coefficients of eq. (12) obtained from the GJ angular distributions $\cos\vartheta_{\mathrm{bK}}^{\mathrm{RpK}}$ for six bins of the Kp invariant mass with equal widths (lower figure). The coefficient a_0 is close to 1, it is given in fig. 26. The upper small figure shows the corresponding reduced χ^2 of the fit. The dashed lines are generated with a second degree polynomial fit and have the only purpose to guide the eye.

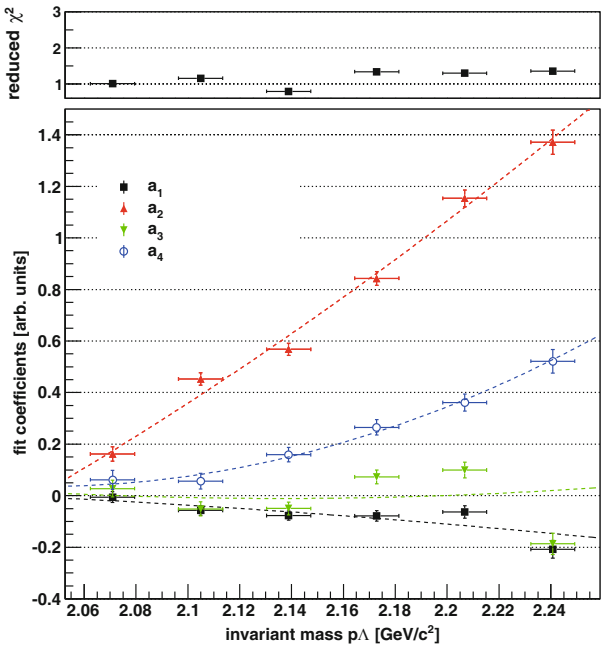

Fig. 18. Fit results of the coefficients of eq. (12) obtained from the GJ angular distributions $\cos\vartheta_{\mathrm{bp}}^{\mathrm{R}\Lambda\mathrm{p}}$ for six bins of the pΛ invariant mass with equal widths (lower figure). The coefficient a_0 is close to 1, it is given in fig. 27. The upper small figure shows the corresponding reduced χ^2 of the fit. The dashed lines are generated with a second degree polynomial fit and have the only purpose to guide the eye.

No specific behavior of the angular momentum composition of the KΛ invariant mass is detected, which could be related to nucleon resonances. Therefore, this distribution seems to be the wrong tool to detect the influence of nucleon resonances. The invariant mass spectra, which contain the Λ, which is the heaviest particle of the reaction in study, show both a nearly linear increase of the a_2 coefficient with the invariant mass and a nearly quadratic increase of the a_4 coefficient. For all three invariant masses the odd coefficients are close to zero, thus indicating that the angular distributions are almost symmetric.

6 Summary

More than 200000 events of the reaction pp $\rightarrow$ pKΛ with a beam momentum of 2.95 GeV/c are analyzed. The angular distributions of the final state particles in the cm system exhibit different characteristics. They are analyzed in dependence on cm momentum by a fit of Legendre polynomials. While the Legendre coefficient a_2 of the Λ distribution rises with the third power of the cm momentum, the coefficient a_2 of the proton distribution rises linear with the cm momentum and is approximately constant for values larger than 0.35 GeV/c. The angular distribution of the kaon is nearly constant for all cm momenta.

The threshold effect in the pΛ invariant mass spectrum at the NΣ threshold can be described by a Flatté distribution by assuming a virtual state of pΛ with a mass above the threshold. It is shown by cuts on the pK helicity angle, that the height and the structure of the cusp is nearly constant along the KΛ invariant mass. Therefore, the intensity variations are most likely due to N* resonances decaying into KΛ. The height of the cusp is isotropic in dependence on the kaon cm angle and in dependence on the Gottfried-Jackson angle in the pΛ rest frame.

In the KΛ invariant mass no deviations at the KΣ threshold are found. The upper-limit of a possible threshold effect is estimated to be 0.3 μb. The examination of the dependence of the Gottfried-Jackson angle in the KΛ frame on the KΛ invariant mass compared to the ones of the pΛ and Kp frames exhibits no peculiarities. This indicates that this examination may not be sensitive to effects of N* resonances.

The authors want to thank the COSY crew for the excellent beam preparation, J. Uehlemann and N. Paul for the operation of the demanding LH_2 target. Discussions with J. Haidenbauer and C. Wilkin are gratefully acknowledged. This work was supported by grants from Forschungszentrum Jülich (COSY-FFE), by the European Union Seventh Framework program (FP7/2007-2013) under grant agreement 283286, and by the Foundation for Polish Science through the MPD programme.

Appendix A.

In the appendix the individual fits of the observables, which are separated into bins of a second observable, are shown (see figs. 19 to 27). Inside each figure the fit results and the range of the second observable are given.

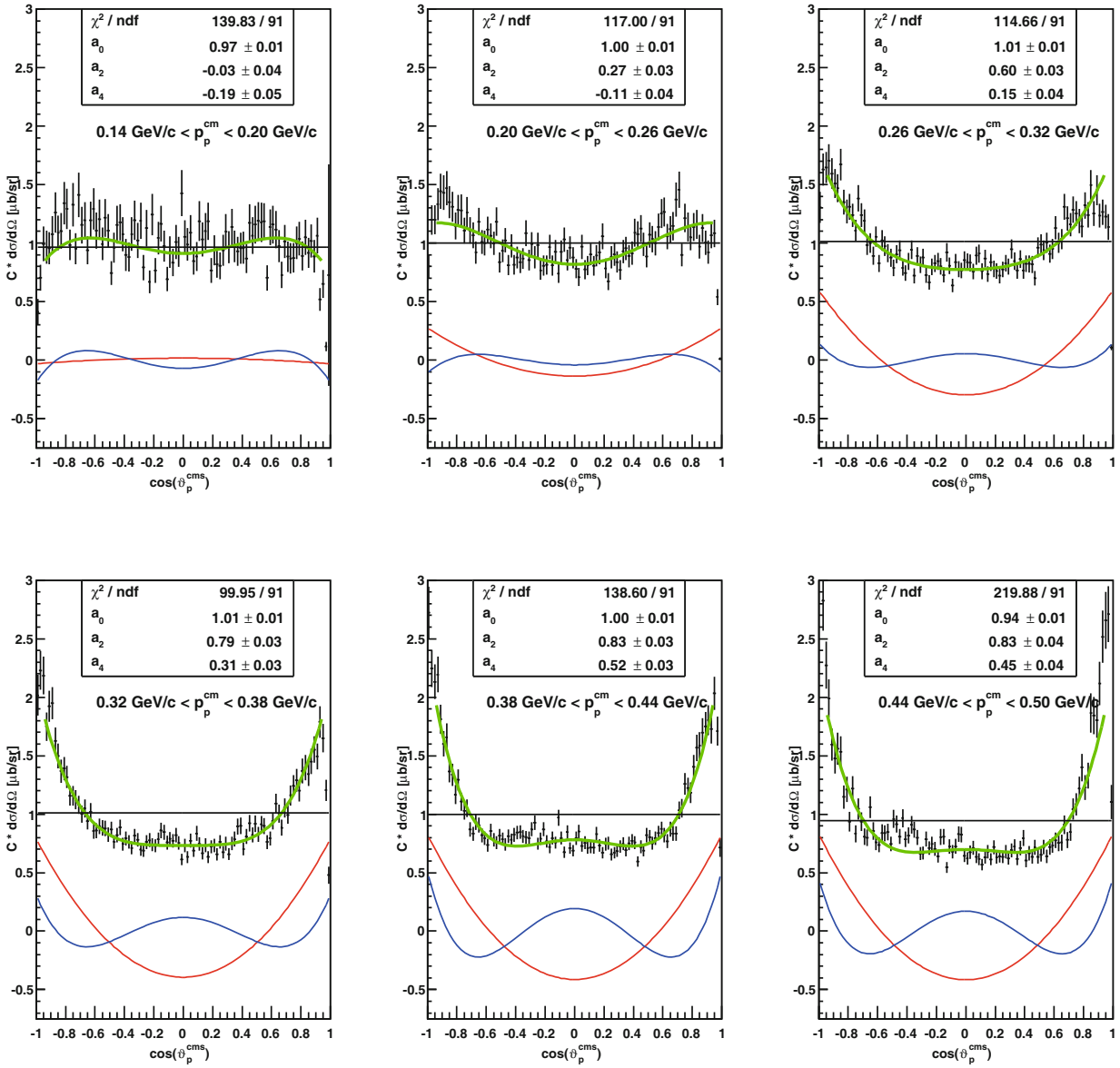

Fig. 19. Proton angular distributions for different ranges of the proton center-of-mass momentum. The green curve shows the fit result. The contributions of the Legendre polynomials P_0, P_2, and P_4, weighted with the corresponding coefficient are plotted in black, red, and blue.

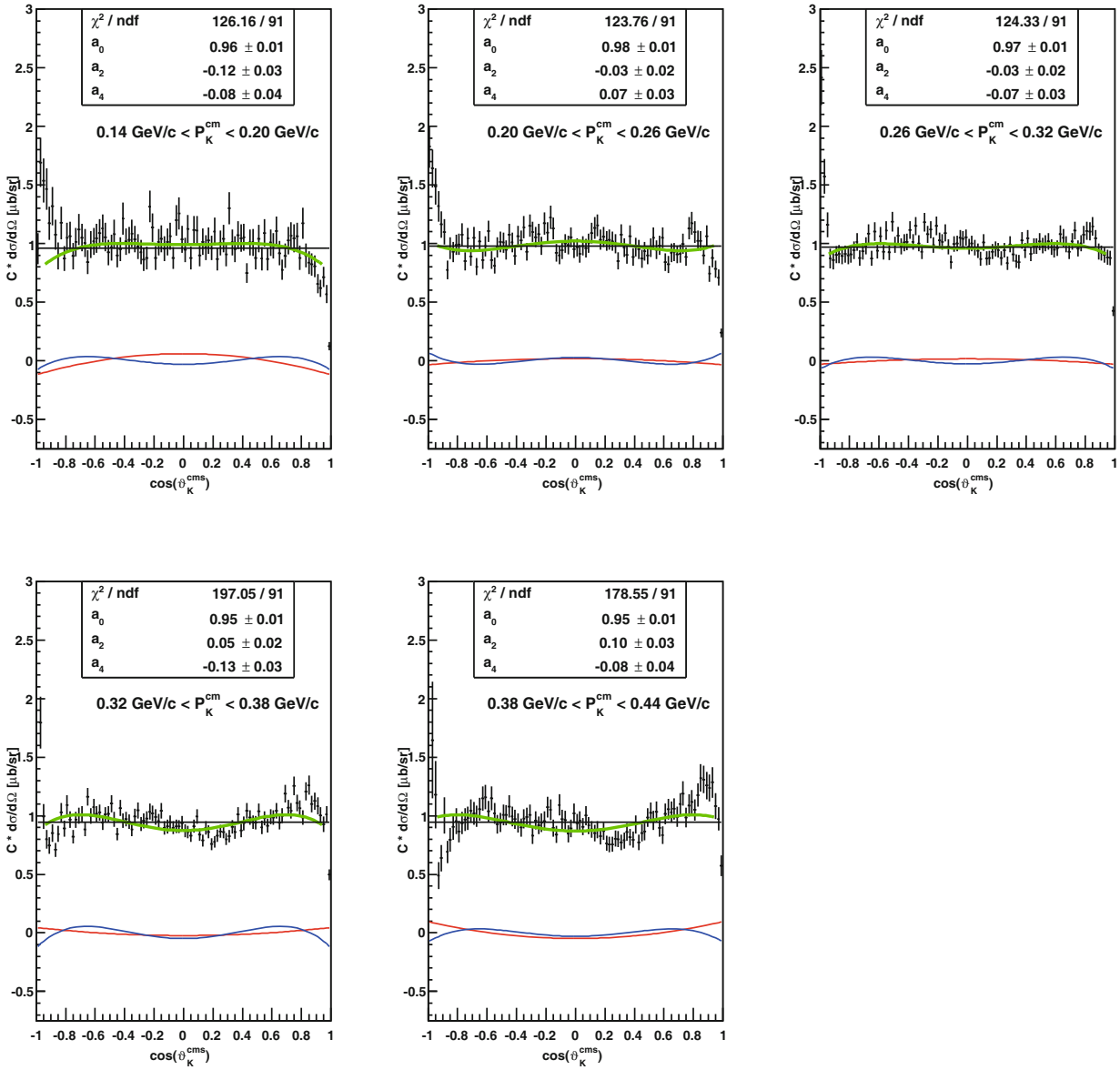

Fig. 20. Kaon angular distributions for different ranges of the kaon center-of-mass momentum. The green curve shows the fit result. The contributions of the Legendre polynomials P_0, P_2, and P_4, weighted with the corresponding coefficient are plotted in black, red, and blue. The last figure is missing, as the maximum kaon momentum is less than $0.44\,\mathrm{GeV}/c$.

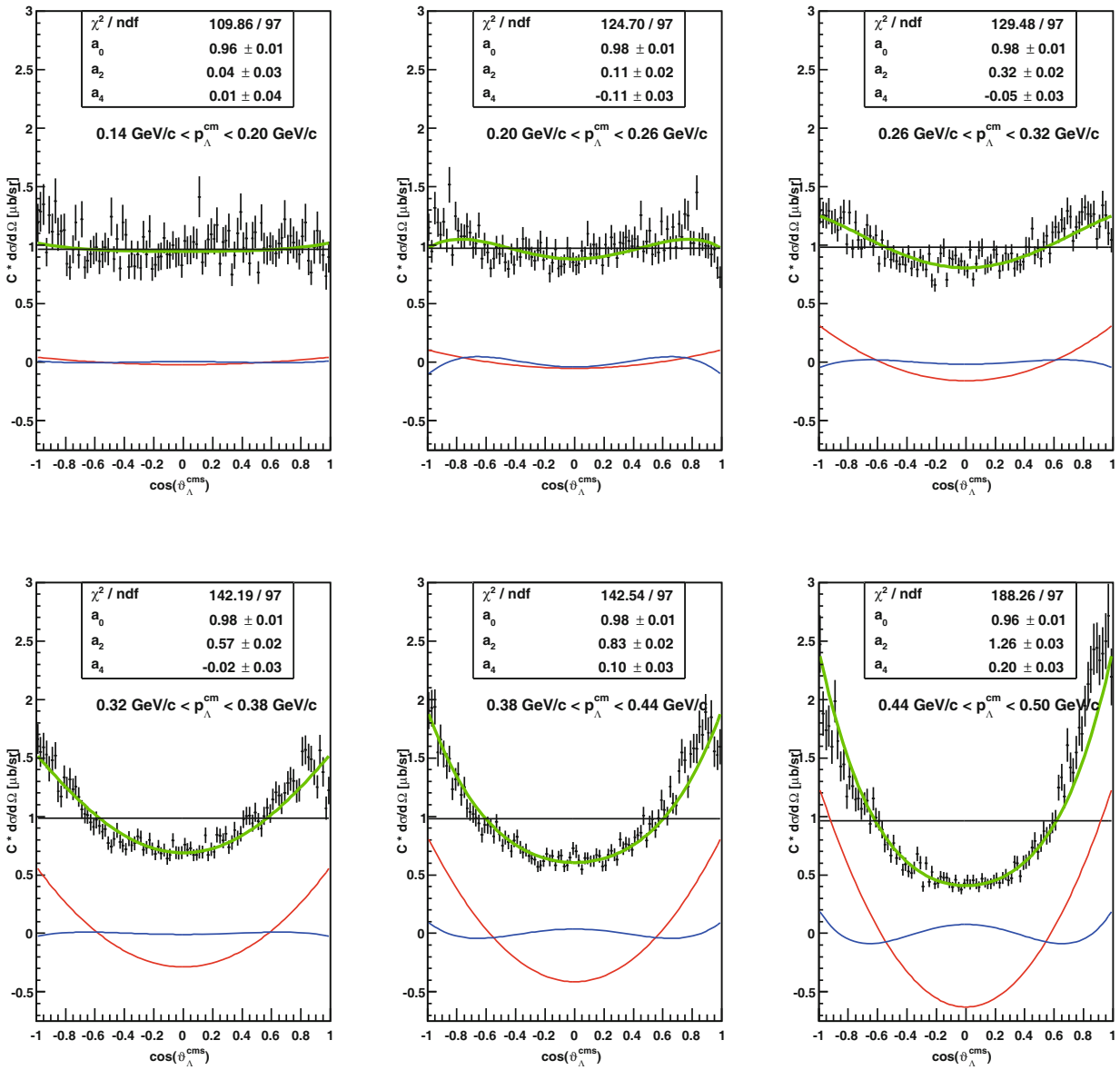

Fig. 21. Λ angular distributions for different ranges of the Λ center-of-mass momentum. The green curve shows the fit result. The contributions of the Legendre polynomials P_0, P_2, and P_4, weighted with the corresponding coefficient are plotted in black, red, and blue.

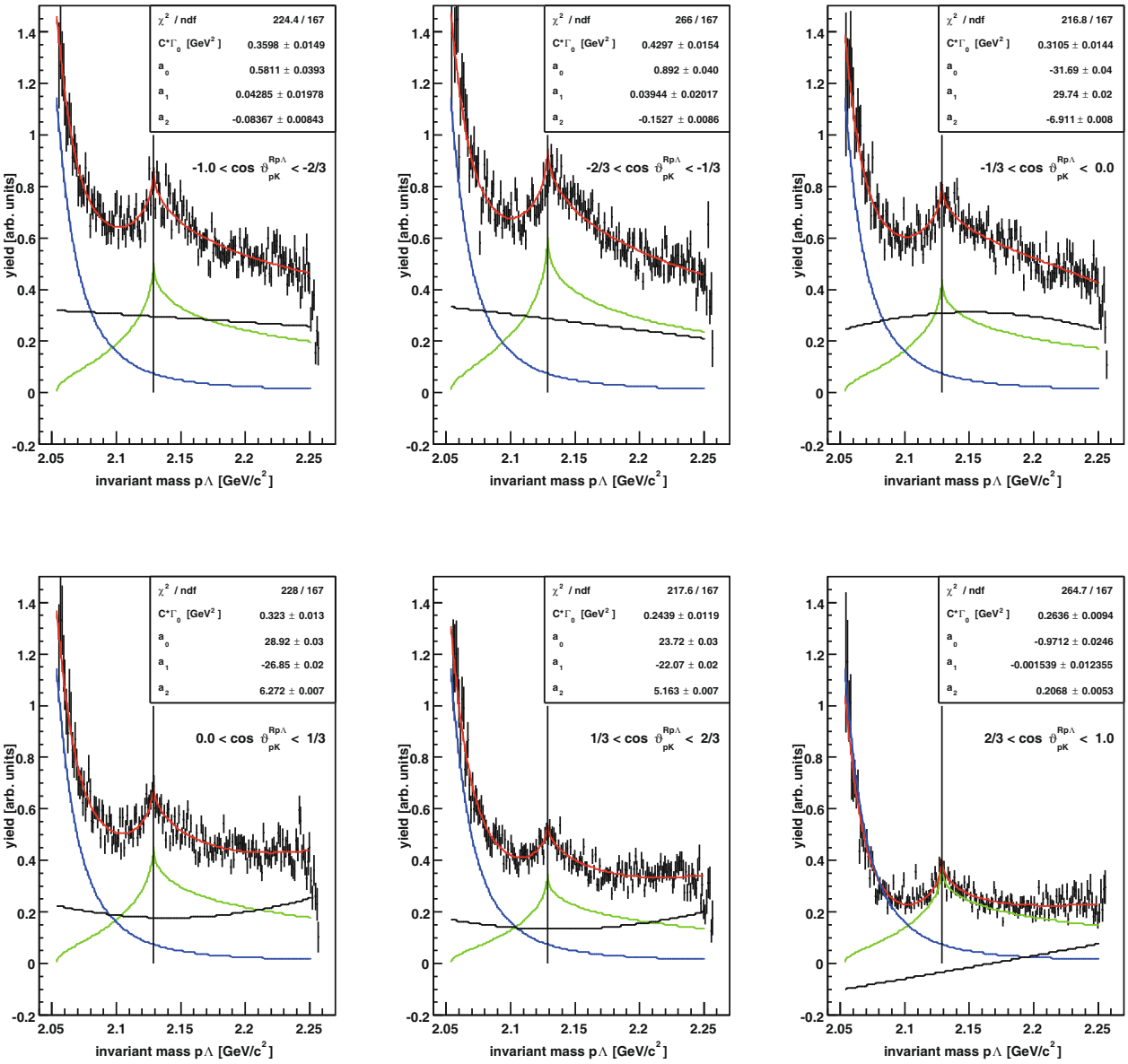

Fig. 22. The pΛ invariant mass distributions are shown for different slices of the Dalitz plot. The slices are generated with cuts in the helicity angle $\cos\vartheta_{\mathrm{pK}}^{\mathrm{Rp}\Lambda}$ as given in the individual plots. The spectra are normalized to 1/6 of the total data set which is shown in fig. 10. The data are shown as points with error bars, the red line is the total fit. The green line is the contribution of the Flatté distribution, where only the height ($C\Gamma_0$) is varied. The blue line is the FSI part with all parameters fixed. The black line is the part of the reflections with freely varying parameters of the second-order polynomial.

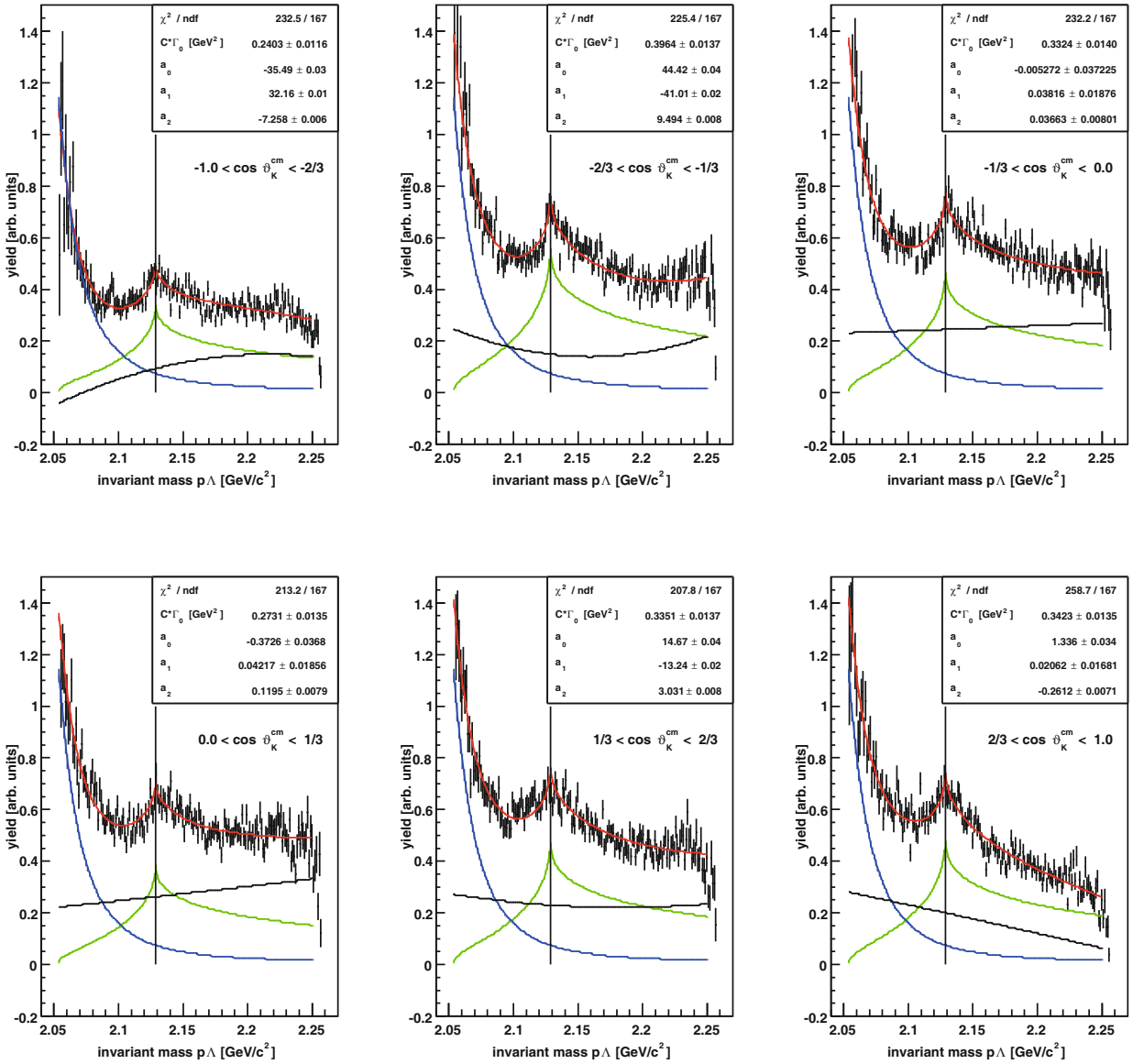

Fig. 23. The pΛ invariant mass distributions are shown for different slices of the kaon cm scattering angle as given in the individual plots. The spectra are normalized to 1/6 of the total data set which is shown in fig. 10. The data are shown as points with error bars, the red line is the total fit. The green line is the contribution of the Flatté distribution, where only the height (CI_0) is varied. The blue line is the FSI part with all parameters fixed. The black line is the part of the reflections with freely varying parameters of the second-order polynomial.

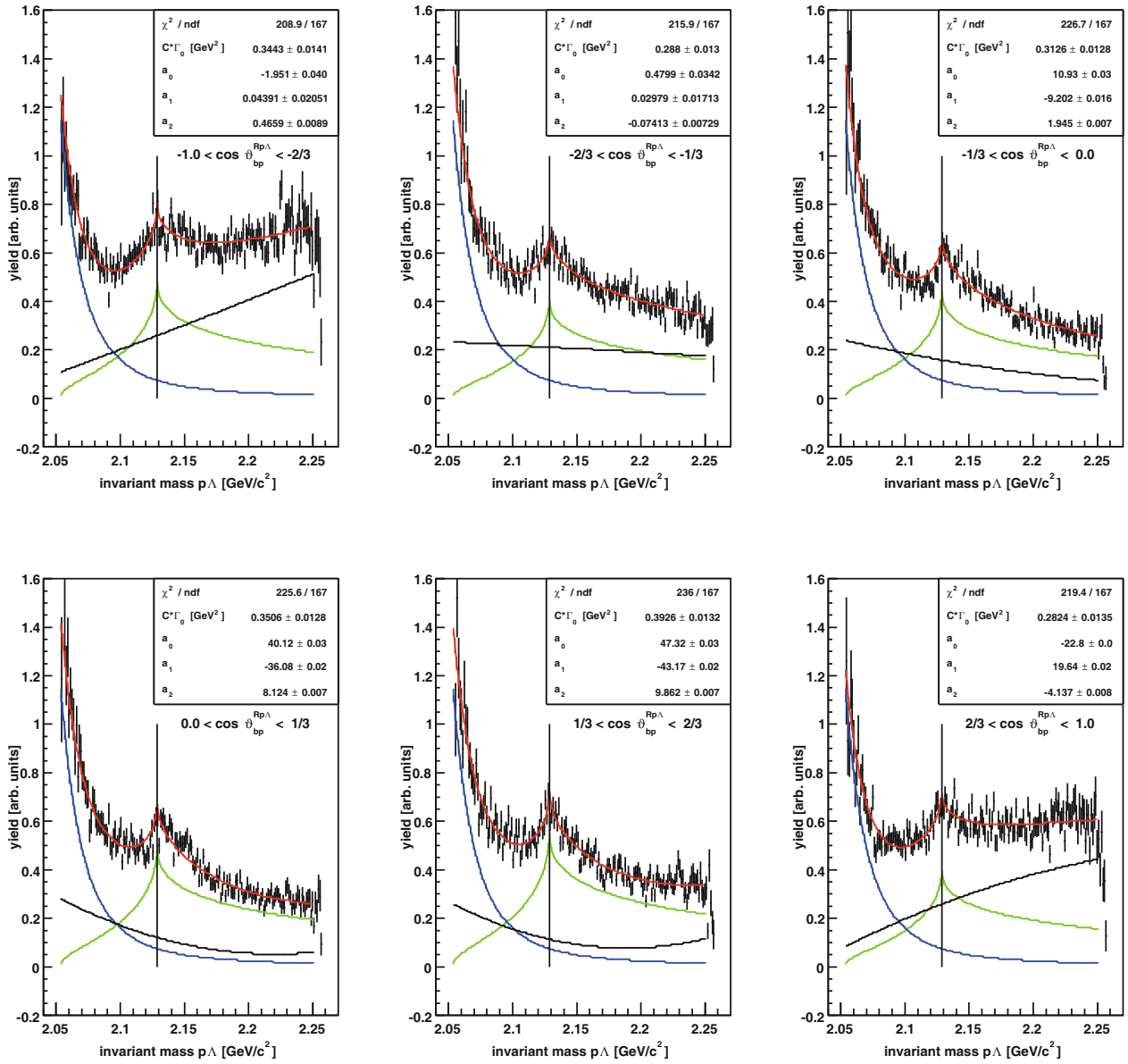

Fig. 24. The pΛ invariant mass distributions are shown for different slices of the proton-beam angle in the GJ pΛ system as given in the individual plots. The spectra are normalized to 1/6 of the total data set which is shown in fig. 10. The data are shown as points with error bars, the red line is the total fit. The green line is the contribution of the Flatté distribution, where only the height ($C\Gamma_0$) is varied. The blue line is the FSI part with all parameters fixed. The black line is the part of the reflections with freely varying parameters of the second-order polynomial.

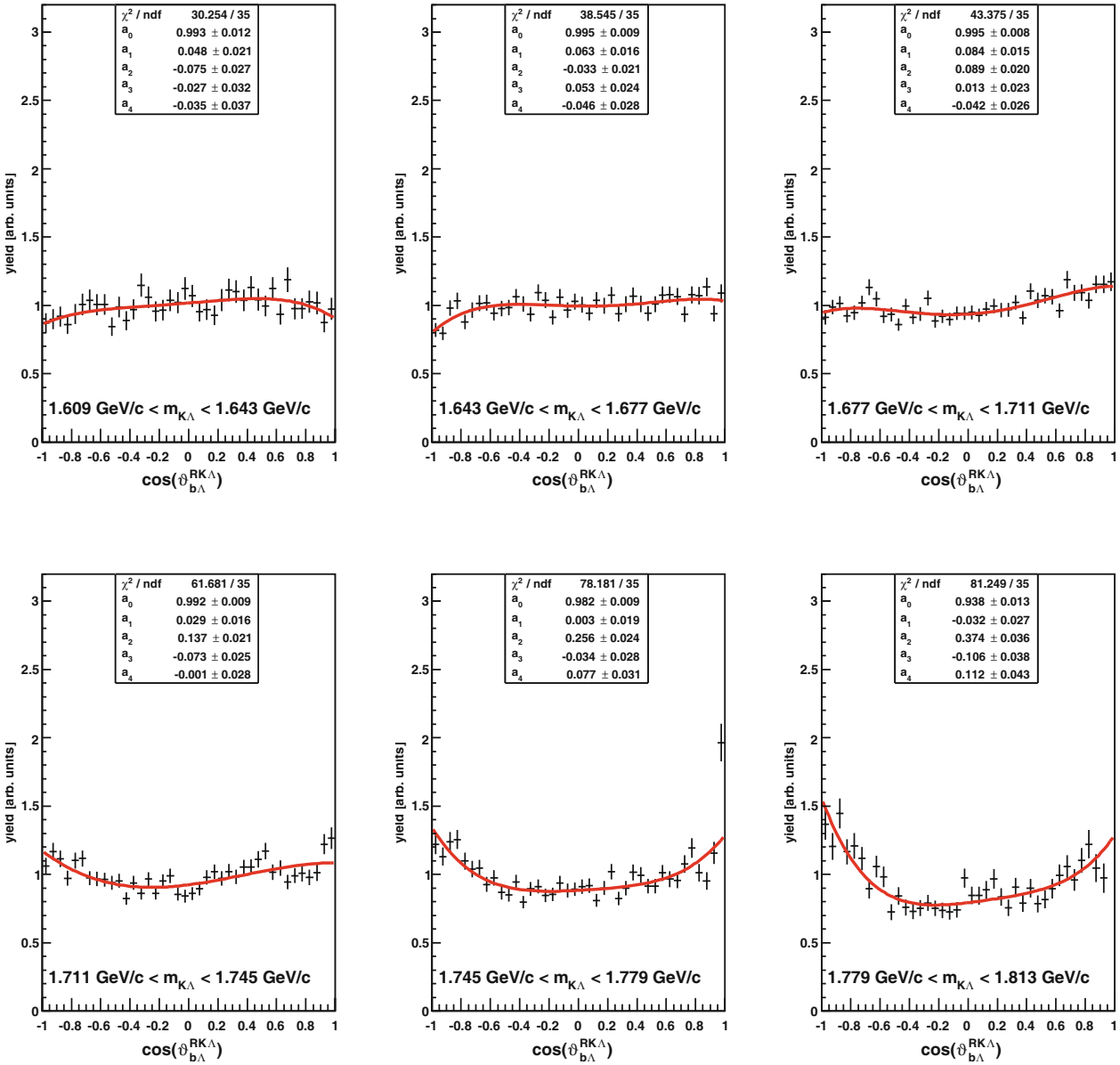

Fig. 25. The GJ angular distribution $\cos\vartheta_{b\Lambda}^{RK\Lambda}$ is shown for six slices of the KΛ invariant mass, the invariant mass ranges of the slices are given in the figures. The data, which are corrected to the acceptance and reconstruction efficiency, are shown by black error bars and the fit result according to eq. (12) is shown by the red line.

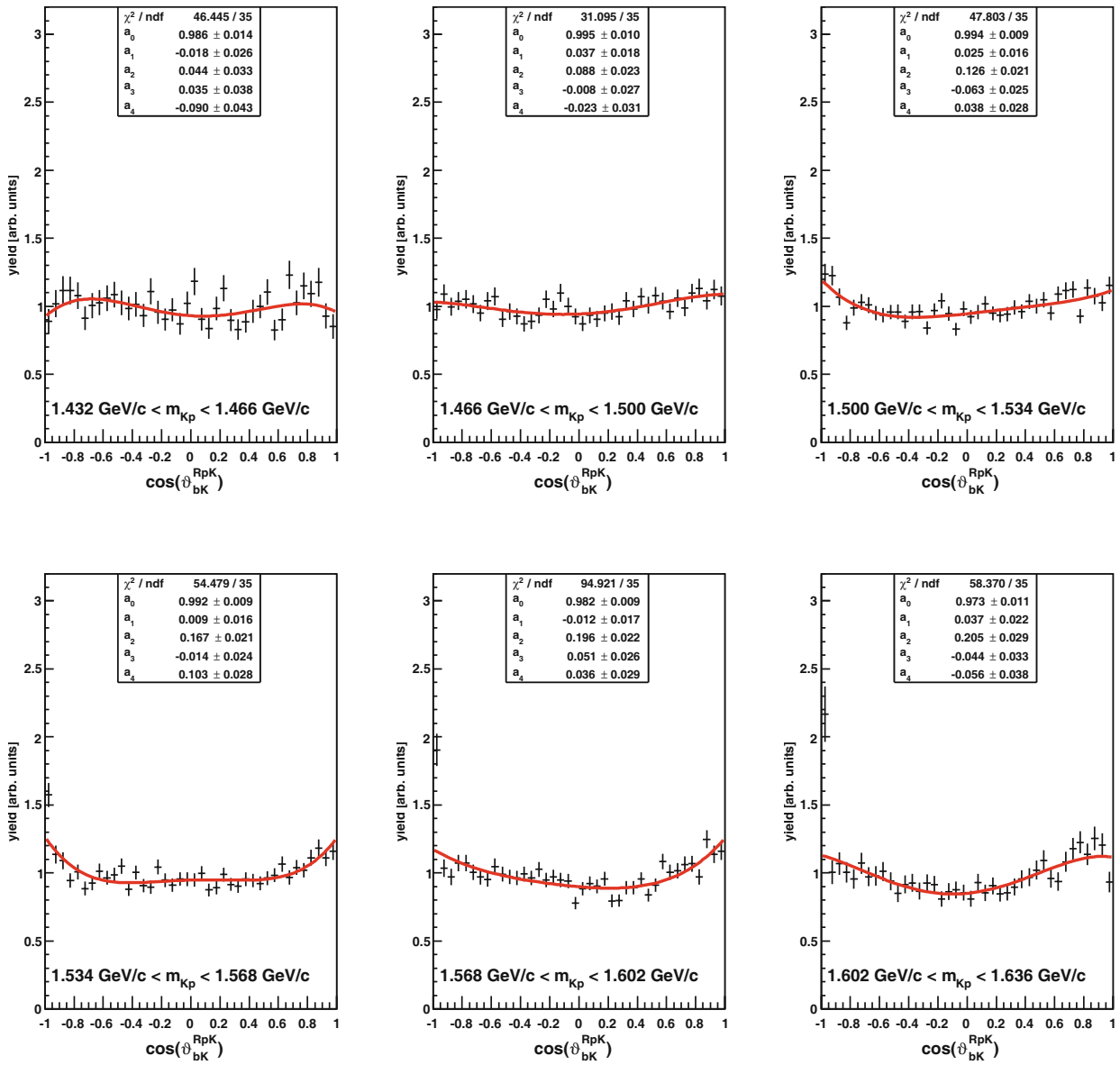

Fig. 26. The GJ angular distribution $\cos\vartheta_{\mathrm{bK}}^{\mathrm{RpK}}$ is shown for six slices of the Kp invariant mass, the invariant mass ranges of the slices are given in the figures. The data, which are corrected to the acceptance and reconstruction efficiency, are shown by black error bars and the fit result according to eq. (12) is shown by the red line.

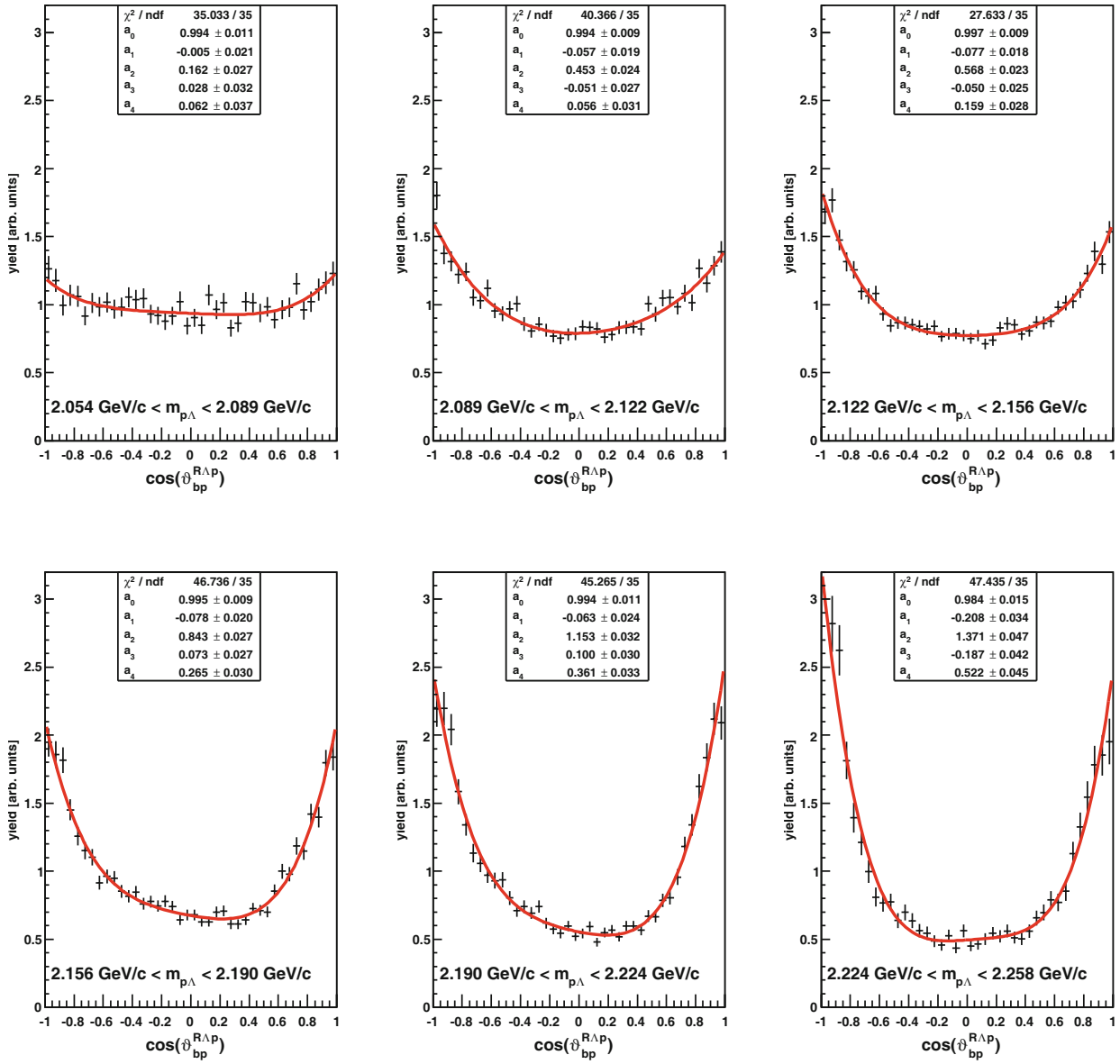

Fig. 27. The GJ angular distribution $\cos\vartheta_{\mathrm{bp}}^{\mathrm{R}\Lambda\mathrm{p}}$ is shown for six slices of the pΛ invariant mass, the invariant mass ranges of the slices are given in the figures. The data, which are corrected to the acceptance and reconstruction efficiency, are shown by black error bars and the fit result according to eq. (12) is shown by the red line.

References

1. E. Ferrari, S. Serio, Phys. Rev. **167**, 1298 (1968).
2. J. Laget, Phys. Lett. B **259**, 24 (1991).
3. A. Sibirtsev, J. Haidenbauer, H.W. Hammer, S. Krewald, Eur. Phys. J. A **27**, 269 (2006).
4. R. Shyam, Pramana **66**, 765 (2006).
5. B. Liu, B. Zou, Phys. Rev. Lett. **96**, 042002 (2006).
6. A. Sibirtsev, K. Tsushima, A.W. Thomas, Phys. Lett. B **421**, 59 (1998).
7. DISTO Collaboration (F. Balestra *et al.*), Phys. Rev. Lett. **83**, 1534 (1999).
8. COSY-TOF Collaboration (S. Abd El-Samad *et al.*), Phys. Lett. B **688**, 142 (2010).
9. COSY-TOF Collaboration (M. Abdel-Bary *et al.*), Eur. Phys. J. A **46**, 27 (2010).
10. T. Rozek *et al.*, Phys. Lett. B **643**, 251 (2006).
11. L. Fabbietti *et al.*, Nucl. Phys. A **914**, 60 (2013).
12. COSY-TOF Collaboration (S. Abdel-Samad *et al.*), Phys. Lett. B **632**, 27 (2006).
13. A. Anisovich, V. Kleber, E. Klempt, V. Nikonov, A. Sarantsev *et al.*, Eur. Phys. J. A **34**, 243 (2007).
14. R. Muenzer, private communications (2015).
15. HADES Collaboration (G. Agakishiev *et al.*), Phys. Lett. B **742**, 242 (2015).
16. A. Gasparyan, J. Haidenbauer, C. Hanhart, Phys. Rev. C **72**, 034006 (2005).
17. J.J. Xie, H.X. Chen, E. Oset, Phys. Rev. C **84**, 034004 (2011).
18. COSY-TOF Collaboration (M. Röder *et al.*), Eur. Phys. J. A **49**, 157 (2013).
19. O.I. Dahl *et al.*, Phys. Rev. Lett. **6**, 142 (1961).
20. T. Tan, Phys. Rev. Lett. **23**, 395 (1969).
21. O. Braun *et al.*, Nucl. Phys. B **124**, 45 (1977).
22. G. Toker, A. Gal, J.M. Eisenberg, Nucl. Phys. A **362**, 405 (1981).
23. A.M. Badalyan, L.P. Kok, M.I. Polikarpov, Yu.A. Simonov, Phys. Rep. **82**, 31 (1982).
24. M. Torres, R.H. Dalitz, A. Deloff, Phys. Lett. B **174**, 213 (1986).
25. COSY-TOF Collaboration (A. El-Samad *et al.*), Eur. Phys. J. A **49**, 41 (2013).
26. B.F. Gibson, E.V. Hungerford, Phys. Rep. **257**, 349 (1995).
27. FINUDA Collaboration (M. Agnello *et al.*), Phys. Rev. Lett. **94**, 212303 (2005).
28. J. Rafelski, B. Muller, Phys. Rev. Lett. **48**, 1066 (1982) Phys. Rev. Lett. **56**, 2334(E) (1986).
29. A. Boehm *et al.*, Nucl. Instrum. Methods A **443**, 238 (2000).
30. M. Dahmen *et al.*, Nucl. Instrum. Methods A **348**, 97 (1994).
31. COSY-TOF Collaboration (P. Wintz), AIP Conf. Proc. **698**, 789 (2004)
32. COSY-TOF Collaboration (S. Jowzaee), Acta Phys. Pol. Suppl. **6**, 1067 (2013).
33. S. Jowzaee, PhD thesis, Jagiellonian University Cracow (2014) `http://juser.fz-juelich.de/record/185801`.
34. R. Castelijns, Tech. rep., COSY-TOF internal documentation (2006).
35. F. Hauenstein, PhD thesis, University Erlangen-Nuernberg (2014) `http://opus4.kobv.de/opus4-fau/frontdoor/index/index/docId/5614`.
36. M. Roeder, PhD thesis, University Bochum (2011) `http://www-brs.ub.ruhr-uni-bochum.de/netahtml/HSS/Diss/RoederMatthias/`.
37. R. Brun, F. Bruyant, A. McPherson, P. Zanarini, *Geant3* (1984), Users Guide, CERN DD/EE/84-1.
38. Particle Data Group Collaboration (K. Olive *et al.*), Chin. Phys. C **38**, 090001 (2014).
39. COSY-TOF Collaboration (M. Abdel-Bary *et al.*), Eur. Phys. J. A **44**, 7 (2010).
40. DISTO Collaboration (F. Balestra *et al.*), Phys. Rev. C **69**, 064003 (2004).
41. DISTO Collaboration (M. Maggiora *et al.*), Nucl. Phys. A **835**, 43 (2010).
42. J. Haidenbauer, private communications (2015).
43. COSY-TOF Collaboration (M. Abdel-Bary *et al.*), Eur. Phys. J. A **16**, 127 (2003).
44. M. Daum *et al.*, Eur. Phys. J. C **23**, 43 (2002).
45. S.M. Flatte, Phys. Lett. B **63**, 224 (1976).
46. V. Baru, J. Haidenbauer, C. Hanhart, A. Kudryavtsev, U.G. Meissner, Eur. Phys. J. A **23**, 523 (2005).
47. R. Brun, F. Rademakers, P. Canal, M. Goto, eConf **C0303241** (2003) see also `http://root.cern.ch/`.